Study of olivine-hosted melt and spinel inclusions from the Song Da ultramafic volcanic suite, northern Vietnam: Compositions, crystallization temperatures, and origin of the low-Ti komatiite-like and high-Ti primary melts

Charbel Kazzy, Alexander V. Sobolev, Valentina G. Batanova, Evgeny V. Asafov, Eero Hanski, Igor S. Puchtel, Andrey E. Izokh, Leonid V. Danyushevsky, Vũ Hoàng Ly, Can Pham-Ngoc, et al.

Chemical Geology 662 (2024) 122219

Contents lists available at ScienceDirect

Chemical Geology

journal homepage: www.elsevier.com/locate/chemgeo

Study of olivine-hosted melt and spinel inclusions from the Song Da ultramafic volcanic suite, northern Vietnam: Compositions, crystallization temperatures, and origin of the low-Ti komatiite-like and high-Ti primary melts

Charbel Kazzy [a], Alexander V. Sobolev [a,*], Valentina G. Batanova [a], Evgeny V. Asafov [b], Eero Hanski [c], Igor S. Puchtel [d], Andrey E. Izokh [e], Leonid V. Danyushevsky [f], Vũ Hoàng Ly [g], Can Pham-Ngoc [g], Tran Tuan Anh [g]

[a] Univ. Grenoble Alpes, Univ. Savoie Mont Blanc, CNRS, IRD, Univ. Gustave Eiffel, ISTerre, 38000 Grenoble, France
[b] Vernadsky Institute of Geochemistry and Analytical Chemistry RAS, Moscow, Russia
[c] Oulu Mining School, University of Oulu, 90014 Oulu, Finland
[d] Department of Geology, University of Maryland, College Park, MD 20742, USA
[e] V.S. Sobolev Institute of Geology and Mineralogy, Novosibirsk, Russia
[f] Friendly Solutions, Australia
[g] Institute of Geological Sciences, Vietnam Academy of Science and Technology, Ha Noi, Viet Nam

ARTICLE INFO

Editor: S Aulbach

Keywords:
Mantle plume
Komatiite
Melt inclusions
Olivine
Spinel
Geothermometry

ABSTRACT

The Permian (~260 Ma) Song Da volcanic suite in Vietnam is one of very few known occurrences of Phanerozoic ultramafic volcanic rocks that are similar in composition to komatiites. Despite continuous efforts to determine the primary melt composition of Song Da ultramafic lavas, the concentrations of the volatile and fluid-mobile elements are still poorly constrained due to widespread alteration and low-grade metamorphism of bulk rocks. This study reports high-precision in-situ major- and trace element abundances in host olivine and inclusions of melt and Cr-spinel from the Song Da ultramafic lavas. Two different types were identified: low-Ti lavas, previously described as komatiites, and newly discovered Ti- and Na-rich picrites. The application of olivine-melt Sc/Y, olivine-spinel Al, and olivine-melt Fe/Mg geothermometers indicates crystallization temperatures of up to 1450 °C for the Song Da low-Ti suite, which are within the range of komatiite crystallization temperatures, and up to 1330 °C for the high-Ti picrites. These conditions correspond to mantle potential temperatures of 1590 °C and 1450 °C, respectively. The estimation of oxygen fugacity, based on V partitioning between olivine and melt and Fe^{2+}/Fe^{3+} between spinel and melt, indicates that low-Ti melts crystallized in a closed system under reducing conditions starting from one to half an order of magnitude below the QFM buffer. The high-Ti melt crystallized at higher oxygen fugacity (ΔQFM +0.5) in a buffered open system. The primary melt of the Song Da komatiites contained 0.7 wt% H_2O, which was likely entrained from the hydrated Mantle Transition Zone (MTZ) by a partially molten plume. Our results indicate that the Song Da low-Ti ultramafic volcanics were likely derived from an ultramafic komatiite-like parental melt with an MgO content between 21 and 23 wt%. It was produced by a high degree (>26%) of partial melting of a depleted mantle source. The high-Ti picrite melt had 17–18 wt% MgO and was produced by a lower degree of partial melting (<9%) in a colder part of the same plume.

1. Introduction

Komatiites are ultramafic volcanic rocks derived from a highly magnesian parental melt (>18 wt% MgO) generated by advanced melting of a peridotitic mantle source at high temperatures (Arndt, 1977; Arndt and Brooks, 1980). The highest temperature of the source

* Corresponding author.
E-mail address: alexander.sobolev@univ-grenoble-alpes.fr (A.V. Sobolev).

https://doi.org/10.1016/j.chemgeo.2024.122219
Received 5 April 2024; Received in revised form 8 June 2024; Accepted 10 June 2024
Available online 11 June 2024

has been thought to be a feature of mantle plumes rising from the core-mantle boundary (Loper and Lay, 1995; Labrosse, 2002; Rost et al., 2005). Therefore, komatiites may serve as a tool to understand the composition of the deep mantle (Campbell et al., 1989; McDonough and Ireland, 1993; Arndt et al., 2008). Another characteristic feature of komatiites is the olivine spinifex texture indicating fast crystallization of a superheated high-MgO melt (Arndt, 1977; Faure et al., 2006). Komatiites mostly formed during the Archean when the mantle temperature was higher than that of the present-day mantle (Herzberg et al., 2010). The only well documented example of olivine spinifex-textured Phanerozoic komatiites are the Cretaceous (89 Ma) komatiites from Gorgona Island off the coast of Colombia (e.g., Echeverria, 1980). In addition, upper Permian olivine-phyric ultramafic lavas with a komatiite-like composition have been reported from the Song Da area in northwestern Vietnam (Polyakov et al., 1991, 1998; Balykin and Petrova, 2000; Hanski et al., 2004; Izokh et al., 2005).

Numerous studies have been conducted on ultramafic lavas of the Song Da volcanic suite (Polyakov et al., 1991, 1996, 1998; Hanski et al., 2004; Wang et al., 2007; Balykin et al., 2010; Anh et al., 2011), although these rocks were altered during several tectonic events that transported the Song Da block from the main Emeishan flood basalt province to its present position in NW Vietnam. Based on the chemical composition, Polyakov et al. (1991) proposed that the low-Ti Song Da suite is, in fact, a komatiite-basaltic komatiite suite similar to those in Archean greenstone belts. This idea was further developed by Hanski et al. (2004), whose conclusion that these rocks are Phanerozoic komatiites was based, in addition to the bulk rocks composition, on the composition of olivine phenocrysts and the following two assumptions: (1) The water content in the parental melt was $\leq$0.03 wt% and, thus, these melts crystallized at high temperatures, and (2) the oxygen fugacity during crystallization of the melt was low and, thus, the high forsterite content of up to 93 mol% of the olivine phenocrysts reflects a high MgO content of the melt from which this olivine crystallized. Based on these assumptions, the parental melt in equilibrium with the most MgO-rich olivine was estimated to have an MgO content of 22–23 wt%. Hence, the authors concluded that these rocks are Phanerozoic komatiites. However, the rocks do not contain olivine spinifex texture, which is commonly considered a characteristic feature of a rock to be classified as komatiite (e.g., Arndt and Nisbet, 1982) and, according to their olivine-phyric texture, they were emplaced as a mixture of olivine crystals and basaltic melt.

The origin of komatiites and the water content in their mantle source have long been debated. The most widely accepted hypothesis is that these rocks formed in high-temperature mantle plumes (Campbell et al., 1989; Campbell and Griffiths, 1992; Herzberg, 1992, 1995; McDonough and Ireland, 1993; Nisbet et al., 1993; Arndt et al., 1998; Sobolev et al., 2016, 2019; Sossi et al., 2016; Asafov et al., 2018; Waterton and Arndt, 2023; Puchtel and Arndt, 2024). Recently, it has been shown by direct measurements of olivine- and spinel-hosted melt inclusions that the parental melts of komatiites from the Gorgona island, Abitibi, Belingwe, and Barberton greenstone belts contain between 0.2 and 0.9 wt% H_2O and show high (>1000) H_2O/Ce ratios (Shimizu et al., 2001; Kamenetsky et al., 2010; Gurenko et al., 2016; Sobolev et al., 2016, 2019; Asafov et al., 2018, 2020). These elevated water contents have been attributed to entrainment of H_2O from the Mantle Transition Zone (MTZ) by partially molten plumes (Sobolev et al., 2016, 2019).

The presence of high-Ti basalts and picrites has been reported from several large igneous provinces (LIP), such as the Siberian Traps (Ryabov et al., 1985) and the Karoo Continental Flood Basalts (Sweeney et al., 1991). This is also true for the Emeishan LIP, which contains both high-Ti and low-Ti volcanic suites (Xu et al., 2001; Xiao et al., 2004; Zhang et al., 2019).

The goal of this study is to obtain detailed information on the primary melt compositions and crystallization conditions of Song Da low-Ti and high-Ti magmas by determining major element compositions and water contents of olivine-hosted melt inclusions, as well as compositions of Cr-spinel inclusions and host olivine phenocrysts.

2. Geological background

Southeast Asia is formed from an arrangement of small continental blocks, such as the Yangtze Block, Indochina Block, Simao terrane, Sibumasu terrane, and West Burma terrane, which are divided by suture zones or fault lines (Metcalfe, 2002). The Song Da district in northern Vietnam is limited by the Ailao Shan-Red River Fault to the northeast and the Song Ma suture to the southwest. It is situated between the Yangtze Block and the Indochina Block (Fig. 1) and its crystalline basement is represented by Archean and Proterozoic complexes (Lan et al., 2000, 2001; Nam et al., 2003). These are overlain by Carboniferous strata followed by Permian limestones, on which the basalts and picrites lie (Anh et al., 2011).

According to Chung et al. (1998), the Song Da suite formed as part of the Emeishan LIP, but was moved some 600 km away from its original location. This happened in the Oligo-Miocene (22–27 Ma) during the collision between India and Asia, which created the Ailao Shan-Red River fault (Chung et al., 1997, 1998; Hanski et al., 2004; Ali et al., 2010). The mafic-ultramafic volcanic rocks of the Song Da suite have been subdivided chemically by Xu et al. (2001) into the high-Ti and low-Ti types. This dichotomy has been explained by derivation from different mantle sources and by different degrees of lithospheric contamination of the two magma types (Wang et al., 2007).

Currently, outcrops of Song Da ultramafic lavas and subvolcanic bodies are heavily altered, fragmented, and submerged underwater of the reservoir of the Son La hydro-electric power station constructed in 2005–2010. Thus, most studies of Song Da magmatic rocks including that of Hanski et al. (2004) rely on detailed geological reconstructions by the Russian-Vietnamese teams published in the 1990's (Balykin et al., 1996; Polyakov et al., 1991, 1996, 1998). According to these reconstructions, the volcanic rocks of the Song Da zone formed in a continental rift environment, and the low-Ti suite is overlain by a high-Ti suite. The few occurrences of pillow textures in several basaltic lava flows (mainly of the high-Ti suite) suggest their eruption underwater.

The age of the Song Da magmatism is Permo-Triassic, but different dating methods have provided somewhat varying age estimates. Polyakov et al. (1996) reported an age of 257 $\pm$ 24 Ma based on the Rb—Sr method; Tran et al. (2008) reported an age of 258.5 $\pm$ 1 Ma based on the $^{40}Ar/^{39}Ar$ method, and Hanski et al. (2004) reported an age of 270 $\pm$ 21 Ma using the Re—Os method. Balykin et al. (1996) obtained a Rb—Sr age of 257 $\pm$ 7.2 Ma for Song Da komatiitic clinopyroxene separates from the northwestern side of the rift zone. More recently, Tang et al. (2015) published a U—Pb age of 256.2 $\pm$ 1.4 Ma for zircons from a volcanic sequence in the Binchuan area in the southern part of the Emeishan LIP, and 258.5 $\pm$ 3.5 Ma for a Baimazhai picrite located northwest of Jinping, at the northern tip of the Song Da volcanic zone. Consequently, ages between 255 and 258 Ma (late Permian) are currently considered as the age range for the mafic and ultramafic magmatic rocks in the Song Da rift zone and several other nearby regional magmatic formations (e.g., Tran et al., 2015; Usuki et al., 2015). These ages closely align with the most precise estimates of the emplacement of the Emeishan LIP of between 257.6 $\pm$ 0.5 Ma and 259.5 $\pm$ 0.5 Ma (Shellnutt, 2014).

3. Samples

In this study, we analyzed olivine and spinel grains from 9 thin sections of olivine-phyric komatiites described by Hanski et al. (2004). We also present olivine, spinel, and melt inclusion compositions from our new collection of olivine-phyric Song Da rocks from the Pa Uan district (SD22–2-1, SD22–2-2, SD22–4-2, SD22–13-3 and SD22–13-4) (Fig. 1). These samples are rare, occasionally relatively fresh pieces of fragmented lava flows or thin subvolcanic bodies without clear contacts. All studied samples are olivine-phyric and contain altered interstitial

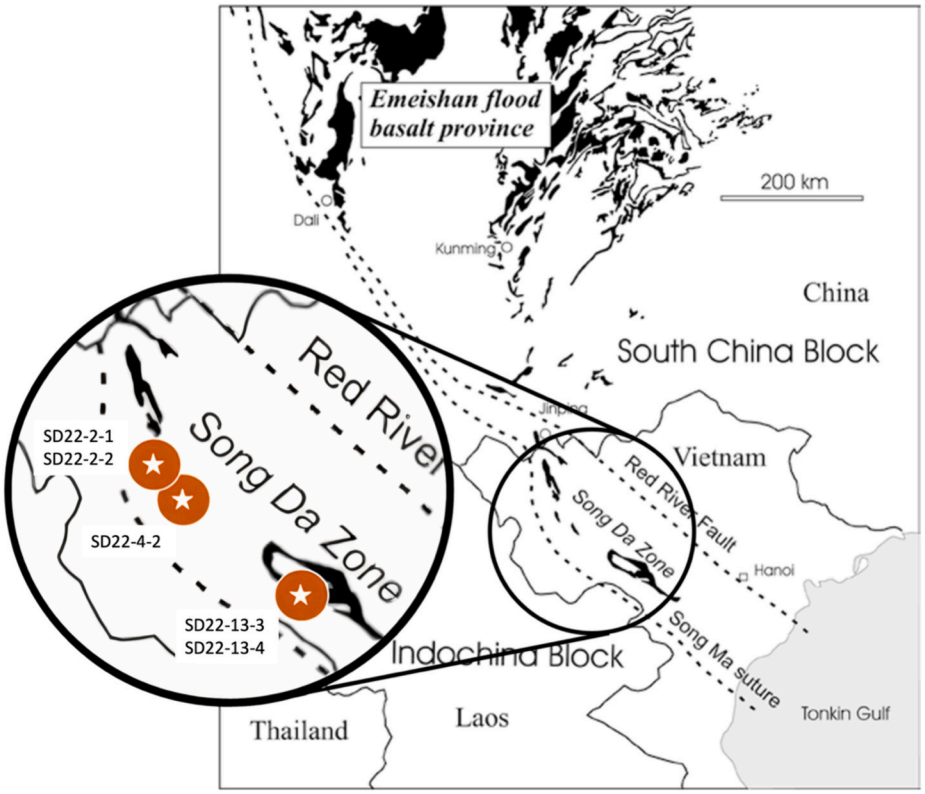

Fig. 1. Geological sketch map of the Song Da zone in north-eastern Vietnam relative to the Emeishan flood basalts in its current position (modified after Hanski et al., 2004). Orange circles represent the locations of sample collection SD22.

glass and residual glass in olivine-hosted melt inclusions (Fig. 2e,f) confirming their volcanic origin. Olivine phenocrysts (antecrysts) of all samples contain numerous inclusions of Cr-spinel and partly crystallized melt. Their chemical compositions confirmed that the studied samples belonged to the known Song Da ultramafic lavas suites (Fig. 3 and Fig. 4).

Sample SD22–13-4, which represents a high-Ti picrite, is an olivine cumulate, containing partly serpentinized olivine phenocrysts up to 1.75 mm in size. The fine-grained groundmass contains microlites of Ti-rich augite, K-bearing nepheline, anorthoclase, albite, titanomagnetite, and altered glass (Fig. 2a, Supplementary Table 4).

All other samples (SD22–2-1, SD22–2-2, SD22–13-3 and SD22–4-2) are from the low-Ti suite. They are also olivine cumulates with partly serpentinized olivine grains up to 2 mm in size and a fine to coarse crystalline groundmass composed of augite, plagioclase, magnetite, and altered interstitial glass (Fig. 2c, d). We also present data for melt inclusions hosted by olivine from sample VS6–1 (Nicklas et al., 2019).

4. Methods

4.1. Sample preparation

The samples were grinded in an automatic grinder, cleaned, sieved, and separated into 2 size fractions of 200–500 μm and 500–800 μm. Fresh olivine was found in the 200–500 μm fraction and was handpicked under a binocular microscope. This fraction was placed in open platinum ampoules and heated in a vertical high-temperature Nabertherm furnace at Vernadsky Institute of Geochemistry in Moscow, Russia. Ampoules were heated for 3 min to up to 1350 °C at 1 atm of C-O-H gas mixture corresponding to the QFM buffer and were then dropped in water-filled glass for instantaneous quenching. Heating temperatures were carefully chosen for each sample to ensure a complete melting of daughter phases in melt inclusions along with a minimum loss of volatile elements through the host olivine via diffusion. The quenched olivine grains were mounted in epoxy to search for melt inclusions. Only melt inclusions that are >25 μm in size were selected. The average size of the inclusions was 37 μm, with a few exceptions being >60 μm. Some melt inclusions are completely homogenized, others have a shrinkage bubble and residual spinel. The shape of the inclusions is spherical or ellipsoidal (Fig. 2). Decrepitated (cracked) inclusions are recognizable due to the ratio of the bubble size to that of the inclusion size, which is significantly higher than the average ratio resulting from the pressure release inside the decrepitated inclusion during heating at 1 atm. Only visually uncracked melt inclusions were chosen for this study. Further filtering was applied based on the composition of the inclusions, which will be detailed in the following sections. Host olivine grains were polished until the melt inclusions were exposed on the surface and ready to be analyzed.

4.2. Electron probe microanalysis

The JEOL JXA-8230 and JXA-iHP200F electron microprobes at the ISTerre, University Grenoble Alps (Grenoble, France), were used for major and trace elements analyses of olivines, spinels and melt inclusions. The ZAF matrix correction procedure was applied to all measurements.

Olivine grains were analyzed at an accelerating voltage of 25 or 20 kV with a probe current of 500 and 900 nA and probe diameter of 1–2 μm using the high-precision analytical procedure from (Batanova et al., 2015, 2018). Olivine reference material MongOL sh11–2 (Batanova et al., 2019) was analyzed as an unknown sample three times for every 30–40 points of olivine analysis to verify analytical precision and accuracy and to correct for any possible instrumental drift (Sobolev et al., 2007). Major elements (Mg, Fe, and Si) were analyzed by energy dispersive spectrometer (EDS), while trace elements were analyzed by wavelength dispersive spectrometers (WDS). The detection limit for

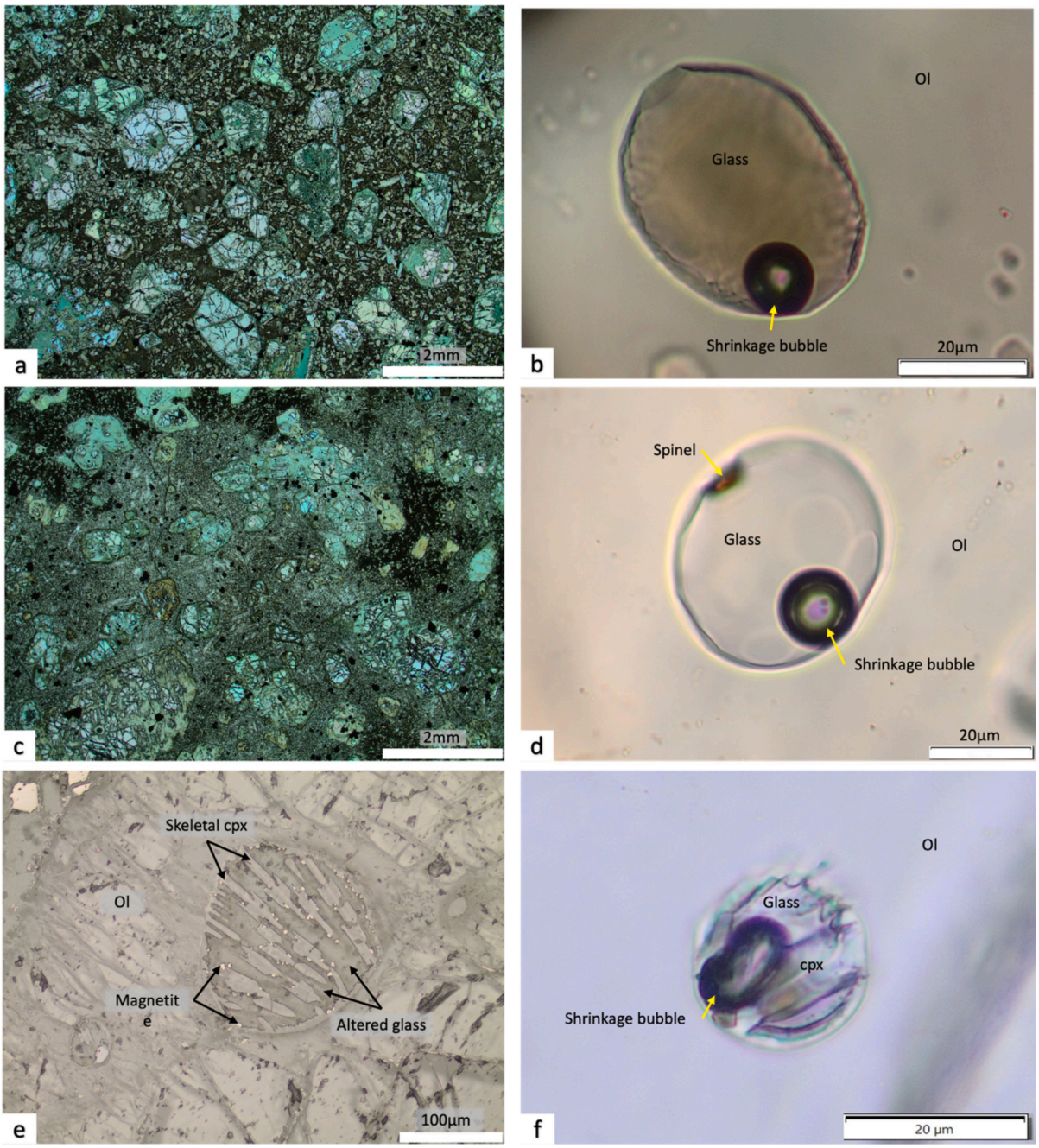

Fig. 2. Photomicrographs of samples (a) SD22–13-4 (high-Ti) and (c) SD22–4-2 (low-Ti), from the Song Da district in transmitted, cross-polarized light. (b) and (d) are images of homogenized melt inclusions from high (SD22-13-4-ol13)- and low-Ti (SD22-4-2-ol9) samples, respectively, containing shrinkage gas babbles and residual spinel (d). (e) and (f) are images of partly crystalized melt inclusions in olivine. (e) is exposed on the surface altered inclusion in altered olivine: useless for homogenization (sample SD22–13-3, low-Ti); (f) is unaltered melt inclusion isolated in the fresh fragment of olivine: advantageous for homogenization (sample SD22–4-2). Sampling locations are presented in Fig. 1.

minor elements, based on three standard deviations of background is typically <20–10 ppm. The representative analyses are reported in Table 1, the reproducibility of MongOL sh11–2 is in supplementary Table 8.

Cr-spinel was analyzed at an accelerating voltage of 15 kV and a probe current of 20 or 50 nA, with a probe diameter of 1 and 2 µm using the analytical method from Batanova et al. (2011). The reproducibility of the reference materials is reported in Supplementary Table 10.

Melt inclusion analyses were performed at accelerating voltages of 15 and 20 kV, probe currents of 12, 20, and 100 nA, and a probe diameter of 5 and 10 µm (e.g., Sobolev et al., 2016) for 9 to 11 min. Two reference materials, GOR132 and VG-2, were analyzed as unknowns for every 30 to 40 points (The reproducibility of the reference materials is reported in Supplementary Table 9). The importance of adding VG-2 reference material is to ensure the accuracy for volatile elements, such as K, P, Cl, and S. In a cracked melt inclusion, Cl, S and Na contents drop due to the pressure decrease down to 1 bar, while in a closed system, concentrations of Cl, S, and Na are around 0.012, 0.015, and 1.2 wt%, respectively, and are kept relatively high by internal pressure. The representative analyses are presented in Table 1. All data are reported in Supplementary Table 2.

The totals of oxides of some olivines and melt inclusions differ from 100 wt% due to the tilted surface of the sample because each olivine with exposed inclusion is mounted individually in the final mount.

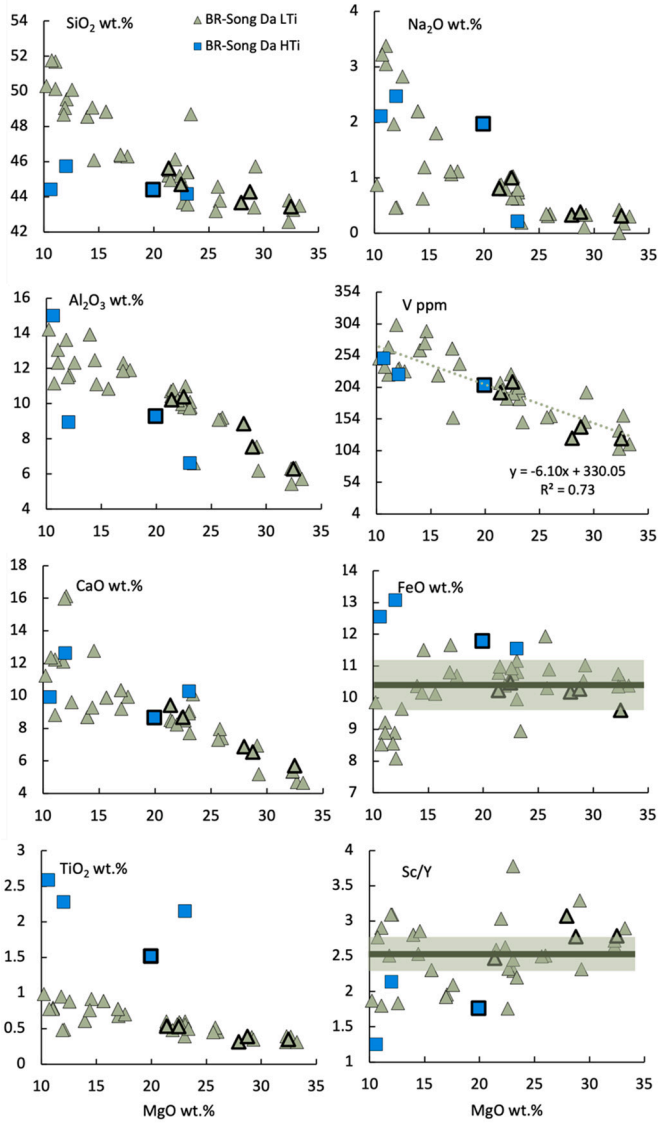

Fig. 3. Bulk-rock compositions of samples from the Song Da region. Data are from this study and Hanski et al. (2004), Wang et al. (2007), Balykin et al. (2010), Anh et al. (2011), and Nicklas et al. (2019). Song Da LTi = Song Da low-Ti. Song Da HTi = Song Da high-Ti. Studied rocks are shown by symbols with bold outlines.

Fortunately, this does not affect the proportions of elements, which is evident from Supplementary Fig. 1, where we plotted all measured Song Da olivines. There is no correlation between the total and sum of cations, and all analyses of olivine are within ±0.3% of the ideal sum of cations of 3.000. However, to be conservative, we reject analyses with a total of over 102 wt%.

4.3. RAMAN microscopy

Raman Horiba LABRAM Soleil (ISTerre, Grenoble, France) was used for analysis of H_2O in melt inclusions. To quantify the water content, we made two calibrations for two different lasers (Supplementary Fig. 2) using a set of natural and artificial glasses with FTIR-measured H_2O contents. The first calibration corresponds to the calibration of the blue laser with a wavelength of 473 nm. This requires a 1800 grooves/mm grating that was used with a hole of 100 μm and a laser power of 19 mW for 60s of exposure time. The second calibration corresponds to the green laser with a wavelength of 532 nm, requiring a 1800 grooves/mm

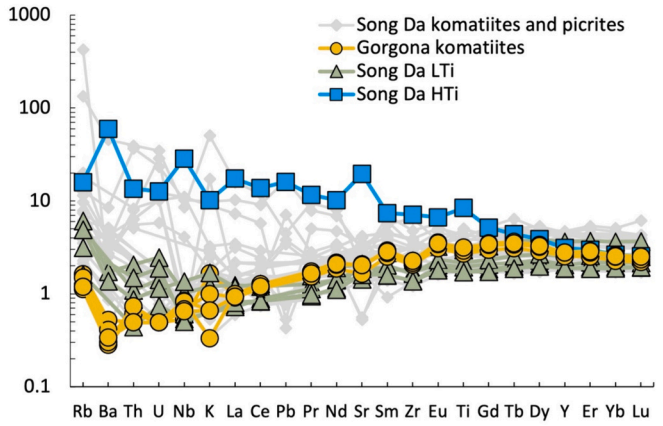

Fig. 4. Spider diagram for Song Da low-Ti and high-Ti samples (color coded symbols), with corresponding data being represented in Supplementary Table 5. Gorgona komatiite data are from Kamenetsky et al. (2010) and Song Da komatiite and picrite (grey symbols) data are from Hanski et al. (2004), Wang et al. (2007), Balykin et al. (2010), Anh et al. (2011), and Nicklas et al. (2019). Song Da LTi = Song Da low-Ti. Song Da HTi = Song Da high-Ti.

grating that was used with a pinhole of 200 μm a laser power for 18 mW for 60s of exposure time. Denoise filter, a feature of Labspec6, was applied to reduce the background signal without affecting the shape of the peaks. Once the filter is applied, a linear baseline on the water bend was anchored at 3125 and 3800 cm^{-1}. Results of water calibration are shown in Supplementary Fig. 2 and the data are presented in Supplementary Table 6.

4.4. Laser ablation ICP-MS

Trace element abundances in olivine were obtained in ISTerre, Grenoble, France, by LA-ICP-MS using a RESOlution SE instrument equipped with an ATL 193 nm excimer laser of 5 ns pulse width, S-155 Laurin Technic ablation cell and squid. Olivine samples were ablated using 38 μm ablation spot, a repetition rate of 10 Hz and fluence of 7 J cm^{-2}. A five-shot pre-ablation surface cleaning and 35 s wash-out preceded each measurement of blank of 30 s and ablation of 40 s. The carrier gas was He (0. 31–0.33 l min^{-1}) mixed with Ar (1.0 l min^{-1}) before introduction into the mass-spectrometer. An Agilent 8900 ICP-QQQ-MS was coupled to the laser and used in no-gas mode. The mass-spectrometer was tuned for a ThO/Th ratio of <0.1 and a U/Th ratio of 1–1.02 using a line ablation on the NIST SRM 612. Twenty-one masses were analyzed (^{7}Li, ^{23} Na, ^{25}Mg, ^{27}Al, ^{29}Si, ^{31}P, ^{23}Ca, ^{45}Sc, ^{49}Ti, ^{51}V, ^{53}Cr, ^{55}Mn, ^{57}Fe, ^{59}Co, ^{62}Ni, ^{63}Cu, ^{66}Zn, ^{71}Ga, ^{89}Y, ^{90}Zr, and ^{172}Yb). The dwell times ranged from 5 to 100 ms depending on expected abundances of isotope giving a total sweep time of 0.69 s. Calibration was performed on NIST 612 for all trace elements except for P, for which BCR-2G was used. Fe, Mg, Si, Ni, Mn, and Ca were calibrated on olivine reference material MongOl sh11–2 (Batanova et al., 2019). Mass ^{25}Mg was used as the internal standard. Calibration reference materials were analyzed twice with each 15 analyses of unknown, using the same conditions as unknown for all reference samples. Data were reduced using the LADR (https://norsci.com/?p=ladr; Norris and Danyushevsky, 2018) software. For matrix effect correction for trace elements, BCR-2G and GSD -1 G were used as secondary reference materials. The details of this approach are discussed in (Batanova et al., 2019). Conventional approaches (Longerich et al., 1996) and normalization to 100% total of oxide components (Liu et al., 2008) were used for quantification. Olivine reference material MongOl sh11–2 was run once as unknown with each 14 analyses to verify calibration, matrix effect correction and final accuracy and precision of olivine analyses (see supplementary Table 7 for reproducibility of this reference material). Repeated measurements of Mongol sh11–2 also showed that interference correction at ^{31}P and ^{45}Sc

Table 1
Representative compositions of Song Da low-Ti (1–9) and high-Ti (10−13) melt inclusions along with their host olivine composition and average primary melt composition (14–15).

	SD22–4-2-ol11	SD22–4-2-ol3	SD22–4-2-ol43	SD22–2-2-ol5	VS6–1-ol-GL1-B2–1	SD22–13-3-ol22	VS6–1-M7322-OlBL5	SD22–2-2-ol17	VS6–1-M3-OL-A3	SD22–13-4-ol16	SD22–13-4-ol8	SD22–13-4-ol12	SD22–13-4-ol11	Average PM low-Ti (87 analyses)	Average PM high-Ti (15 analyses)
Melt inclusion	1	2	3	4	5	6	7	8	9	10	11	12	13	14	15
SiO_2	45.99	47.07	48.54	48.85	49.09	50.74	48.09	48.44	48.30	40.45	41.36	42.71	42.85	46.85	41.97
2SE	*0.17*	*0.13*	*0.14*	*0.10*	*0.13*	*0.13*	*0.18*	*0.01*	*0.17*	*0.12*	*0.12*	*0.13*	*0.00*	*0.12*	*0.40*
TiO_2	0.591	0.488	0.468	0.492	0.360	0.437	0.683	0.784	0.712	2.074	2.017	2.029	1.949	0.464	1.918
2SE	*0.001*	*0.013*	*0.004*	*0.011*	*0.006*	*0.015*	*0.003*	*0.017*	*0.023*	*0.024*	*0.026*	*0.026*	*0.003*	*0.016*	*0.107*
Al_2O_3	10.05	10.13	10.22	11.02	12.08	10.71	14.02	13.70	14.69	10.24	12.76	12.29	11.10	9.86	10.65
2SE	*0.06*	*0.05*	*0.06*	*0.09*	*0.07*	*0.06*	*0.06*	*0.06*	*0.09*	*0.05*	*0.07*	*0.07*	*0.09*	*0.09*	*0.32*
Fe_2O_3	1.01	1.04	1.11	1.14	1.24	1.47	1.43	1.45	1.60	2.62	2.69	2.70	2.64	0.96	2.53
2SE	*0.004*	*0.008*	*0.006*	*0.007*	*0.005*	*0.003*	*0.008*	*0.03*	*0.015*	*0.020*	*0.016*	*0.016*	*0.020*	*0.002*	*0.016*
FeO	9.66	9.64	9.58	9.54	9.45	9.25	9.28	9.26	9.13	9.43	9.37	9.36	9.42	9.30	9.12
2SE	*0.04*	*0.08*	*0.05*	*0.06*	*0.04*	*0.02*	*0.05*	*0.18*	*0.09*	*0.07*	*0.06*	*0.06*	*0.07*	*0.02*	*0.06*
MnO	0.102	0.103	0.110	0.105	0.120	0.127	0.113	0.105	0.102	0.047	0.112	0.120	0.085	0.110	0.098
2SE	*0.001*	*0.016*	*0.018*	*0.007*	*0.007*	*0.014*	*0.003*	*0.030*	*0.016*	*0.008*	*0.011*	*0.011*	*0.009*	*0.002*	*0.016*
MgO	21.64	20.68	18.24	17.32	15.00	14.22	12.03	11.91	10.75	18.35	12.45	11.77	16.02	21.82	17.86
2SE	*0.72*	*0.13*	*0.25*	*0.08*	*0.09*	*0.09*	*0.02*	*0.14*	*0.07*	*0.12*	*0.08*	*0.08*	*0.42*	*0.07*	*0.08*
CaO	9.11	8.81	9.65	9.38	10.12	10.86	11.81	11.58	12.04	10.44	11.58	12.41	10.13	8.65	10.28
2SE	*0.05*	*0.03*	*0.11*	*0.01*	*0.02*	*0.04*	*0.04*	*0.19*	*0.13*	*0.03*	*0.04*	*0.04*	*0.13*	*0.08*	*0.67*
Na_2O	1.029	1.106	1.210	1.357	1.553	1.536	1.674	1.794	1.680	5.354	5.952	5.083	4.486	1.153	4.32
2SE	*0.026*	*0.035*	*0.032*	*0.063*	*0.057*	*0.048*	*0.053*	*0.034*	*0.083*	*0.079*	*0.098*	*0.087*	*0.011*	*0.025*	*0.25*
Cr_2O_3	0.095	0.147	0.158	0.139	0.260	0.229	0.037	0.055	0.057	0.042	0.085	0.063	0.049	0.119	0.043
2SE	*0.013*	*0.023*	*0.014*	*0.029*	*0.006*	*0.020*	*0.027*	*0.001*	*0.017*	*0.014*	*0.018*	*0.018*	*0.011*	*0.010*	*0.012*
K_2O	0.016	0.012	0.021	0.029	0.022	0.022	0.032	0.038	0.035	0.627	0.912	0.887	0.816	0.021	0.728
2SE	*0.001*	*0.002*	*0.001*	*0.002*	*0.002*	*0.002*	*0.002*	*0.001*	*0.005*	*0.005*	*0.007*	*0.007*	*0.002*	*0.001*	*0.028*
Cl	<D.L.	<D.L.	<D.L.	<D.L.	0.003	<D.L.	0.006	<D.L.	<D.L.	0.049	0.083	0.063	0.049	0.003	0.053
2SE	*<D.L.*	*<D.L.*	*<D.L.*	*<D.L.*	*0.001*	*<D.L.*	*0.001*	*<D.L.*	*<D.L.*	*0.002*	*0.003*	*0.003*	*0.001*	*0.0003*	*0.004*
P_2O_5	0.031	0.039	0.046	0.062	0.057	0.038	0.070	0.066	0.061	0.204	0.294	0.354	0.322	0.047	0.334
2SE	*0.007*	*0.005*	*0.001*	*0.002*	*0.008*	*0.006*	*0.002*	*0.012*	*0.017*	*0.008*	*0.011*	*0.012*	*0.011*	*0.003*	*0.117*
S	0.019	0.024	0.010	0.008	0.031	0.009	<D.L.	0.068	0.008	0.076	0.151	0.104	0.064	0.018	0.088
2SE	*0.002*	*0.002*	*0.001*	*0.000*	*0.006*	*0.002*	*<D.L.*	*0.004*	*0.005*	*0.003*	*0.004*	*0.003*	*0.001*	*0.003*	*0.017*
H_2O	0.68	0.74	0.65	0.56	0.65	0.38	0.72	0.820	0.86	0.12	0.42	0.22	0.14	0.64	0.15
2SE	*0.01*	*0.02*	*0.02*	*0.02*	*0.07*	*0.10*	*0.03*	*0.035*	*0.02*	*0.02*	*0.03*	*0.04*	*0.02*	*0.04*	*0.04*
Total	99.9	99.9	99.9	99.9	99.9	99.9	99.9	99.9	99.9	99.9	100.0	99.9	99.8	100.0	100.0
size	70	32	41	40	29	29	41	34	44	53	38	31	52		
Host Olivine															
Fo	93.16	92.69	91.65	91.19	89.99	89.37	88.18	88.05	86.97	93.41	88.97	88.19	92.12	93.30	93.40
2SE	*0.04*	*0.05*	*0.03*	*0.37*	*0.42*	*0.06*	*0.03*	*0.48*	*0.13*	*0.01*	*0.14*	*0.06*	*0.71*		
Al_2O_3	0.0709	0.0833	0.0893	0.0939	0.0938	0.0938	0.0542	0.0809	0.0470	0.0548	0.0380	0.0379	0.0536		
2SE	*0.0042*	*0.0028*	*0.0073*	*0.0024*	*0.0087*	*0.0113*	*0.0058*	*0.0052*	*0.0014*	*0.0094*	*0.0007*	*0.0057*	*0.0061*		
Na_2O	0.0066	0.0067	0.0050	0.0042	#N/A	0.0033	#N/A	0.0063	#N/A	0.0185	0.0160	0.0168	0.0167		
2SE	*0.0009*	*0.0002*	*0.0002*	*0.0010*	*#N/A*	*0.0012*	*#N/A*	*0.0002*	*#N/A*	*0.0039*	*0.0009*	*0.0010*	*0.0040*		
CoO	0.0168	0.0175	0.0181	0.0174	#N/A	0.0200	#N/A	0.0200	#N/A	0.0162	0.0189	0.0201	0.0168		
2SE	*0.0011*	*0.0005*	*0.0003*	*0.0005*	*#N/A*	*0.0001*	*#N/A*	*0.0006*	*#N/A*	*0.0008*	*0.0002*	*0.0003*	*0.0007*		
CaO	0.2876	0.2789	0.2860	0.2823	0.2866	0.2708	0.3261	0.3071	0.3308	0.2221	0.2838	0.4527	0.2531		
2SE	*0.0063*	*0.0089*	*0.0025*	*0.0050*	*0.0076*	*0.0048*	*0.0012*	*0.0032*	*0.0014*	*0.0022*	*0.0073*	*0.0004*	*0.0672*		
P_2O_5	0.0018	0.0064	0.0043	0.0062	#N/A	0.0022	#N/A	0.0048	#N/A	0.0059	0.0083	0.0242	0.0064		
2SE	*0.0005*	*0.0010*	*0.0023*	*0.0036*	*#N/A*	*0.0004*	*#N/A*	*0.0030*	*#N/A*	*0.0006*	*0.0012*	*0.0035*	*0.0020*		
TiO_2	0.0034	0.0046	0.0069	0.0068	0.0046	0.0088	#N/A	0.0071	0.0031	0.0116	0.0089	0.0141	0.0162		
2SE	*0.0004*	*0.0004*	*0.0010*	*0.0007*	*0.0002*	*0.0005*	*#N/A*	*0.0003*	*0.0012*	*0.0003*	*0.0005*	*0.0018*	*0.0019*		
NiO	0.427	0.435	0.412	0.408	0.405	0.356	0.341	0.361	0.344	0.459	0.331	0.328	0.440		
2SE	*0.002*	*0.003*	*0.001*	*0.007*	*0.004*	*0.003*	*0.001*	*0.007*	*0.005*	*0.001*	*0.004*	*0.005*	*0.030*		
MnO	0.112	0.118	0.129	0.132	0.158	0.166	0.184	0.177	0.194	0.109	0.182	0.206	0.125		
2SE	*0.001*	*0.001*	*0.000*	*0.005*	*0.006*	*0.001*	*0.004*	*0.005*	*0.002*	*0.001*	*0.003*	*0.002*	*0.016*		

(*continued on next page*)

Table 1 (*continued*)

	SD22–4-2-ol11	SD22–4-2-ol3	SD22–4-2-ol43	SD22–2-2-ol5	VS6–1-ol-GL1-B2–1	SD22–13-3-ol22	VS6–1-M7322-OlBL5	SD22–2-2-ol17	VS6–1-M3-OL-A3	SD22–13-4-ol16	SD22–13-4-ol8	SD22–13-4-ol12	SD22–13-4-ol11	Average PM low-Ti (87 analyses)	Average PM high-Ti (15 analyses)
Cr_2O_3	0.1246	0.1549	0.1161	0.1127	0.1006	0.0887	0.0472	0.0820	0.0474	0.1078	0.0750	0.0470	0.0907		
2SE	*0.0045*	*0.0042*	*0.0013*	*0.0048*	*0.0058*	*0.0142*	*0.0031*	*0.0047*	*0.0027*	*0.0109*	*0.0039*	*0.0088*	*0.0122*		
MgO	51.75	50.92	50.02	49.49	49.26	48.80	47.87	46.97	46.13	50.18	48.02	47.63	50.44		
2SE	*0.13*	*0.11*	*0.06*	*0.25*	*0.18*	*0.04*	*0.11*	*0.28*	*0.08*	*0.03*	*0.08*	*0.10*	*0.57*		
FeO	6.77	7.16	8.12	8.52	9.77	10.34	11.42	11.36	12.33	6.31	10.61	11.37	7.69		
2SE	*0.06*	*0.04*	*0.02*	*0.35*	*0.42*	*0.07*	*0.03*	*0.45*	*0.14*	*0.00*	*0.14*	*0.05*	*0.67*		
SiO_2	41.70	41.31	40.95	40.77	40.98	41.05	40.43	40.00	39.77	40.31	40.53	40.66	41.17		
2SE	*0.08*	*0.08*	*0.04*	*0.07*	*0.13*	*0.00*	*0.10*	*0.06*	*0.16*	*0.08*	*0.06*	*0.08*	*0.16*		
Total	101.3	100.5	100.2	99.8	101.1	101.2	100.7	99.4	99.2	97.8	100.1	100.8	100.3		

was not required. Integration intervals were carefully chosen to exclude any kind of contamination, such as spinel inclusions under the surface. Preferred reference values from GEOReM database were used for NIST 612, BCR-2G and GSD-1G. The data and 2SE uncertainties are reported in supplementary Table 1.

4.5. Powder preparation and bulk-rock analysis

A fragment of the core for each rock sample was crushed in a hand mortar and pestle to reduce the size of the grains to 5 mm maximum. Crushing was followed by wet grinding using a high-power planetary ball mill at ISTerre, Grenoble, France. The grinded material was dried by freeze drying to obtain a nano-powder with a grain size of <10 μm. Whole-rock analysis was performed by Service d'Analyse des Roches et des Minéraux (SARM) in CRPG Nancy, France by ICP-OES (major elements) and ICP-MS (trace elements). The data are presented in Supplementary Table 5.

4.6. Data processing

Cracked melt inclusions are characterized by a loss of volatile elements, such as Na, Cl, and S. Because the concentrations of Cl and S in all Song Da melt inclusions are close to the detection limit of electron microprobe analysis, we filter decrepitated melt inclusions using Na content. All inclusions that show a drop in Na_2O were filtered out. Post-entrapment correction should be applied to the Song Da melt inclusions due to crystallization of olivine and iron loss. Olivine tends to crystallize over the rims of the melt inclusions, resulting in a compositional gradient caused by Mg—Fe re-equilibration with the host content (Danyushevsky et al., 2000, 2002). All data were recalculated using Petrolog4 software (https://petrologsoftware.com Danyushevsky and Plechov, 2011) assuming a constant amount of total iron in the melt (see below). Fig. 3 shows bulk-rock compositions of different samples from the Song Da region, with data taken from this study and (Hanski et al., 2004; Wang et al., 2007; Balykin et al., 2010; Anh et al., 2011; Nicklas et al., 2019). Most low-Ti rocks follow an olivine control line, indicating a similar parental melt for all these samples. Based on Fig. 3, total iron in the melt is estimated to be 10.6 ± 0.6 wt% for the Song Da low-Ti suite, and 11.8 wt% for the Song Da high-Ti suite.

For samples SD22–2-1, SD22–2-2, SD22–13-3, SD22–4-2, and VS6–1, two models were used for correcting melt inclusion compositions for post-entrapment re-equilibration: those of Danyushevsky (2001) and Herzberg and O'Hara (2002). The melt inclusions in olivine of sample SD22–13-4 are exceptionally rich in Na_2O (>4 wt%, see below), which is out of the calibration range of most models for olivine-melt Fe—Mg equilibrium. Therefore, several models were tested using Petrolog4 to identify the best fitting model for this sample. The starting compositions are experimental glasses from Koshlyakova et al. (2022) with high Na and Ti contents that are similar to those in sample SD22–13-4 melt inclusions. Based on the results presented in Supplementary Fig. 3, the best-fitting model is the one of Weaver and Langmuir (1990), which was used for correcting high-Ti melt inclusion compositions for post-entrapment re-equilibration.

The oxidation state of the system is defined as a function of the olivine composition based on compositions of olivine-hosted spinels (Supplementary Fig. 4). The calculation of (Fe^{2+}/Fe^{3+}) in the melt is estimated from (Fe^{2+}/Fe^{3+}) in spinel as described by Maurel and Maurel (1984). The oxygen fugacity was calculated following the model of Borisov and Shapkin (1990).

4.7. Geothermometry and geobarometry

To estimate the crystallization temperature, we used three geothermometers: 1) Al-in-olivine (Zhang et al., 2023), 2) Fe—Mg partitioning between olivine and melt inclusions (Ford et al., 1983; Danyushevsky, 2001; Herzberg and O'Hara, 2002), and 3) Sc and Y

partitioning between olivine and melt (Mallmann and O'Neill, 2013).

Spinel coexists with olivine during crystallization of the Song Da picrites, and thus the olivine-spinel geothermometer can be applied. Two hundred sixty olivines-spinel pairs were analyzed from 16 samples for the application of the Al-in-olivine geothermometer based on the empirical equation developed by Zhang et al. (2023). The smallest spinel grain analyzed had a size of 5 μm, and the average spinel size was 10 μm. The errors were estimated based on the counting statistics of individual microprobe analyses as 2 standard deviations (2SD). The average relative 2SD on Cr_2O_3 and Al_2O_3 in spinel is 0.45% and 0.32%, respectively. As for olivine, the average relative 2 standard errors (for three analyses) on Cr_2O_3 and Al_2O_3 is 7% and 6%, respectively.

Vanadium concentrations in melt inclusions are affected by the presence of spinels. Therefore, recalculating V from whole-rock compositions based on the correlation between MgO and trace elements from the same rock suite is more reliable. Data used for recalculating V are from Hanski et al. (2004), Wang et al. (2007), Balykin et al., 2010, Anh et al. (2011), and Nicklas et al. (2019) and are presented in Fig. 3. The V content strongly correlates with the MgO in the melt corresponding to the following equation:

$$V\ melt = 355 - 7,07 \times MgO, R^2 = 0.71$$

The Sc/Y ratio of the rocks does not depend on MgO (Fig. 3), which is expected because of an incompatible behavior of both in olivine. Thus, the average ratio of 2.54 was used for low-Ti and high-Ti samples.

To estimate the oxygen fugacity in the melt during crystallization, we used two geobarometers: 1) V partitioning between olivine and melt (Mallmann and O'Neill, 2013) and 2) oxygen fugacity estimated using Petrolog4, based on Fe^{2+}/Fe^{3+} in the melt calculated using the compositions of spinel inclusions, hosted olivines and equation of Maurel and Maurel (1984) together with the model of Borisov and Shapkin (1990).

5. Results

5.1. Bulk-rock compositions

Whole-rock compositional data for the SD22 sample collection are listed in Supplementary Table 5. Fig. 3 represents bulk-rock compositions of different samples from the Song Da region. The studied samples well represent the low-Ti ultramafic suite. The sodium content of the studied high-Ti picrite is much higher than in the previously reported high-Ti picrites (Balykin et al., 2010), but similar to high-Ti basalts. Fig. 4 represents a spider diagram for Song Da low-Ti and high-Ti samples from this study, along with all previously reported data on ultramafic-mafic rocks from the area and representative analyses of Gorgona komatiites. The Song Da low-Ti suite rocks and the Gorgona komatiites are similar in terms of trace element abundances, but differ significantly from the high-Ti picrite, which is enriched in highly incompatible lithophile trace elements and depleted in heavy REE.

5.2. Olivine compositions

Analyses for Song Da olivines are listed in Supplementary Table 1 and shown in Fig. 5. All olivine compositions and their uncertainties represent the mean values and two standard errors of three analyses for each olivine grain. The olivine compositions were filtered to avoid zoning: only olivine compositions with a standard error equal to or less than the error of individual analyses was included. The forsterite content ranges from 82-83 to over 93 mol% in both the low-Ti and high-Ti suites. The maximum Fo contents are 93.32 ± 0.02 wt% in the low-Ti samples and 93.41 ± 0.01 wt% in the high-Ti samples, with both representing the highest Fo values reported so far for the Song Da rocks.

Olivines in the Song Da low-Ti suite have similar minor element contents, while there are significant differences between the Song Da

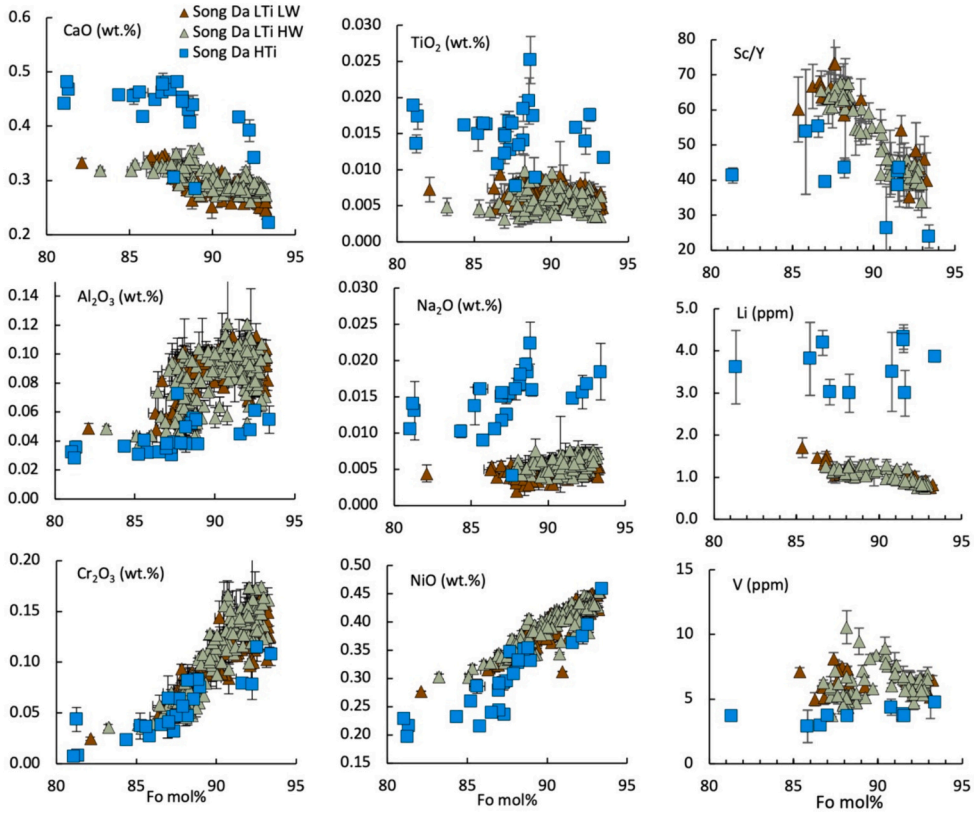

Fig. 5. Olivine compositions from the Song Da rocks. Error bars correspond to 2 standard errors: all oxides and corresponding Fo contents are from EPMA data, others are from LA ICP-MS. Song Da LTi LW = Song Da low-Ti Low Water. Song Da LTi HW = Song Da low-Ti High Water. Song Da HTi = Song Da high-Ti.

low-Ti and high-Ti suites (Fig. 5). The former are lower in Ca, Na, Ti, Mn, Li and higher in Al, Cr, Sc/Y, V, and Ni than the latter at the same Fo content. A notable feature, however, is the partial overlap of the olivine compositions of both suites in contents of Ca, Ti and Na. In Fig. 5, we also use different color coding for olivine from samples of low-Ti suite containing melt inclusions with dominantly high H_2O/K_2O ratio (samples SD22–4-2; SD22–2-2 and VS6–1)-Song Da LTi HW and those samples containing melt inclusions with dominantly low H_2O/K_2O ratio (samples SD22–2-1; SD22–13-3)- Song Da LTi LW.

5.3. Melt inclusion compositions

Analyzing melt inclusions is essential to understanding the evolution of the parental melt of the Song Da rocks. In addition, melt inclusions potentially represent a closed system (except for H), because most volatile and mobile elements are conserved inside the inclusions (Sobolev, 1996; Danyushevsky et al., 2002). Fig. 6 shows H_2O/K_2O, which can be considered as a proxy for the H_2O/Ce ratio, with the latter being widely accepted as a marker of the source composition (Dixon et al., 2017). Primitive mantle-derived and typical mantle plume-derived melts have H_2O/K_2O ratios between 1.0 and 1.2 (e.g. Hauri, 2002; Sobolev et al., 2019), while the Song Da data show a large range from 1 to 60, indicating an enrichment in H_2O relative to the mantle composition.

Fig. 7 represents a compilation of melt inclusion data from Emeishan flood basalts (Zhang et al., 2021). Neither the low-Ti nor the high-Ti Song Da melts have exact analogs among the reported Emeishan melt inclusion compositions. The low-Ti melts are lower in Ti, K and Ca and higher in Al than any other Emeishan melts, with the closest analogue being the Dali suite. The Song Da high-Ti suite is much higher in Na, higher in K and lower in Si than any other melts reported from the Emeishan province.

5.4. Parental melt compositions

Fig. 8 shows parental melt compositions in equilibrium with the most Fo-rich olivine for magmatic suites from different locations in the Emeishan LIP. The MgO content of the parental melt of the Song Da low-Ti suite ranges from 21 to 23 wt%, which is higher than the minimum value for komatiites of 18 wt% (Arndt and Nisbet, 1982). The Song Da low-Ti parental melt overlaps with that of Dali, except for Ti, which is lower in the Song Da suite. The Song Da high-Ti parental melt overlaps with the Lijiang parental melts for all elements except for Na, which is much higher in Song Da.

5.5. Geothermometry

Crystallization temperatures were estimated using three different geothermometers: 1) Al-in-olivine geothermometer, based on the partitioning of Al between olivine and spinel (Zhang et al., 2023), 2) geothermometer based on the Sc/Y partitioning between olivine and melt (Mallmann and O'Neill, 2013), and 3) geothermometer based on the Fe—Mg partitioning between olivine and melt (Ford et al., 1983; Danyushevsky, 2001; Herzberg and O'Hara, 2002). The first geothermometer does not require the knowledge of compositional data of melt inclusions, while the second one is not sensitive to such compositions (using average compositions of melt inclusions instead of individual melt compositions leads to a difference of <10 degrees). The third geothermometer depends on the H_2O content in the melt and assumptions for post-entrapment correction of melt inclusion compositions, as well as on the choice of model for Fe—Mg partitioning between olivine and melt. Thus, we consider the first two geothermometers more reliable than the third one. However, all three geothermometers indicate similar maximum temperatures of crystallization for the most Mg-rich olivines: around 1450 °C for low-Ti suite rocks and close to 1320 °C for the high-Ti picrite. The Sc—Y and Fe—Mg thermometers show a gradual decrease of the calculated temperature with decreasing Fo, while the Al-in-olivine geothermometer indicates decoupling between temperature and Fo for almost half of the measurements. These observations are discussed in section 7.1 below.

5.6. Oxygen fugacity

Fig. 10 represents ΔQFM values (oxygen fugacity compared to the quartz–fayalite–magnetite buffer) calculated using two different methods: 1) vanadium partitioning between olivine and melt (Mallmann and O'Neill, 2013) and 2) Fe^{2+}/Fe^{3+}(melt) based on olivine and spinel compositions (Maurel and Maurel, 1984; Borisov and Shapkin, 1990). Both methods give similar results: at the highest forsterite content, the low-Ti suite yields ΔQFM from −1 to 0 and correlates with forsterite up to ΔQFM +2.5 at 85 mol% forsterite, indicating evolution of oxygen fugacity in a closed system. However, the high-Ti sample yields a constant ΔQFM between +0.5 and + 1, being more oxidized than low-Ti suite and following the evolution of a buffered system.

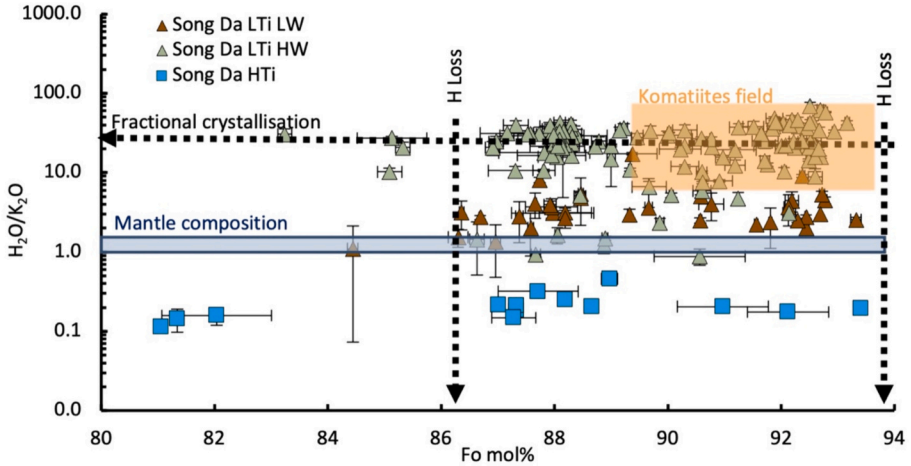

Fig. 6. H_2O/K_2O in melt inclusions after post-entrapment correction. Error bars are 2 standard errors. The H_2O/K_2O ratio of Hawaiian tholeiitic melts and of primitive mantle after (Hauri (2002), and Sobolev et al. (2019). Field of komatiite melts from Sobolev et al. (2016, 2019), and Asafov et al. (2018). Song Da LTi LW = Song Da low-Ti Low Water-melt inclusions from samples SD22–13-3 and SD22–2-1 where melts with low H_2O contents were predominant. Song Da LTi HW = Song Da low-Ti High Water- melt inclusions from samples VS6–1, SD22–4-2 and SD22–2-2 where melts with high H_2O contents were predominant. Song Da HTi = Song Da high-Ti.

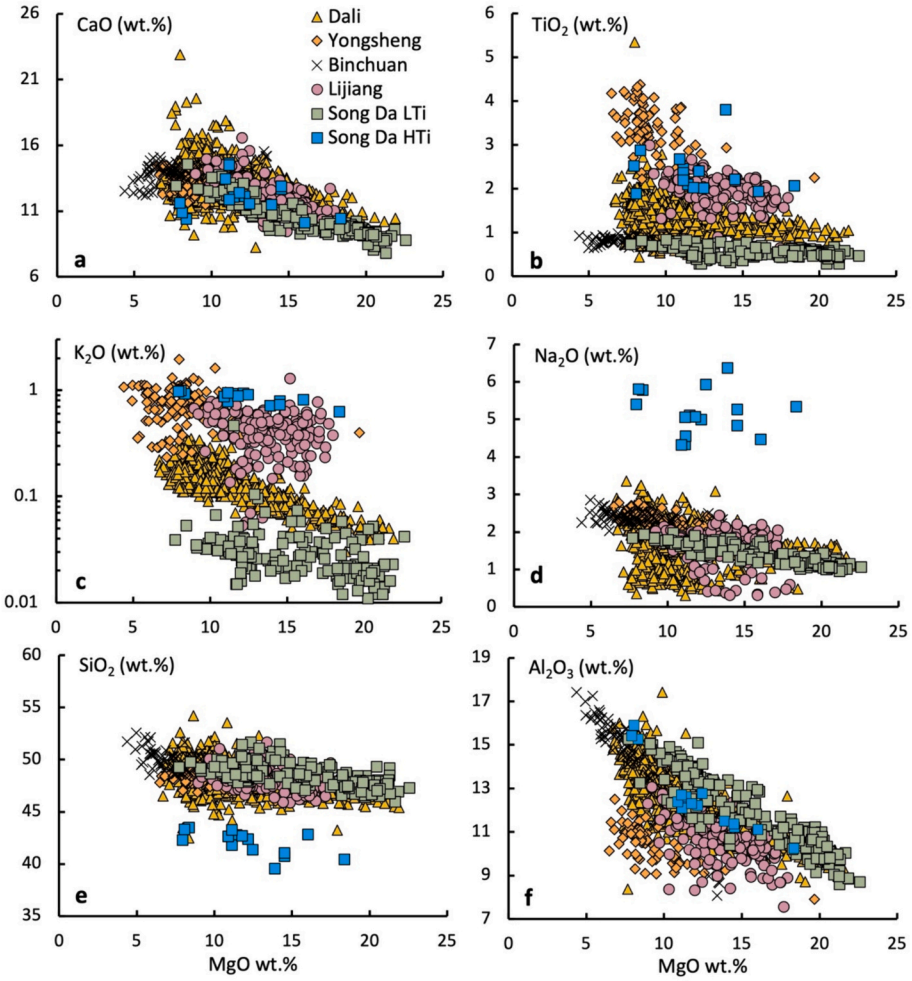

Fig. 7. Melt inclusion data from Emeishan flood basalts. All data are corrected for post-entrapment modification using Petrolog4 software (https://petrologsoftware.com Danyushevsky and Plechov, 2011). The calculation was done using the model of Ford et al. (1983) except for Song Da low-Ti suite rocks (Song Da LTi) that was calculated using the model of Danyushevsky (2001) using measured H_2O contents and Song Da high-Ti suite rocks (Song Da HTi) that was calculated using the model of Weaver and Langmuir (1990). Data of Yongsheng and Binchuan melt inclusions are from Kamenetsky et al. (2012). Dali melt inclusion data are from Hanski et al. (2010), Ren et al. (2017), and Zhang et al. (2019), Lijiang data from Zhang et al. (2021), and Song Da data are from this study.

6. Discussion

6.1. Crystallization temperatures

The olivine-spinel geothermometer, which is based on the partitioning of Al between olivine and spinel, can be used to assess the crystallization temperature of primitive magmas (Zhang et al., 2023). In an ideal case of olivine crystallization, temperature and forsterite content should be positively correlated, as shown by the data from the Sc—Y and Fe—Mg geothermometers for the low-Ti lavas (Fig. 9). However, there are some conditions under which the Fo content and temperature can decouple. 1) If olivine that crystallized at a high temperature is cooled in a cumulate layer with a low amount of interstitial melt, diffusion in olivine will affect Al more than Fe and Sc because of the low concentrations of these elements in the interstitial melt compared to their concentrations in olivine. Therefore, the temperature calculated from Al in olivine may vary despite the absence of variation in the forsterite content and Sc/Y ratio of olivine. The Sc/Y ratio of olivine and its Fo content in this case will retain the memory of the high-temperature stage. 2) When olivine crystallizes in a convecting magma chamber, diffusion of Mg, Fe, Sc, and Y in the system will instantaneously equilibrate olivine and melt compositions. The Al diffusion rate in olivine is >10 times lower than those of Mg, Fe, Sc, and Y (Spandler and O'Neill, 2010), hence, the forsterite content and Sc/Y ratio may change while olivine retains its original Al content and, thus, the information about its initial crystallization temperature. This can explain decoupling of Fo and T measured by the olivine-spinel Al geothermometer, as well as the strong correlation between Fo and the Mg—Fe and Sc—Y temperatures.

Taking into account their measured H_2O contents, Sobolev et al. (2016, 2019) and Asafov et al. (2018) estimated that most komatiites start to crystallize in the temperature range between 1400 and 1500 °C, which are higher than those of most modern mantle plume-derived melts and mid-ocean ridge basalts (Zhang et al., 2023). The highest crystallization temperature of the Song Da low-Ti suite, calculated from the three geothermometers, is around 1450 °C and is consistent with the crystallization temperatures of komatiites.

Song Da high-Ti melts started to crystalize at a temperature of around 1320 °C (Fig. 9), which is significantly lower than that of the low-Ti melts, but higher than that of present-day mid-ocean ridge basalts (Zhang et al., 2023).

6.2. Origin of low-Ti Song Da melts: mantle plume vs subduction zone setting

The origin of ultramafic magmas has long been debated. The first school of thought defended the hypothesis that komatiites formed in high-temperature mantle plumes via dry melting (McDonough and Ireland, 1993; Nisbet et al., 1993; Arndt et al., 1998; Walter, 1998;

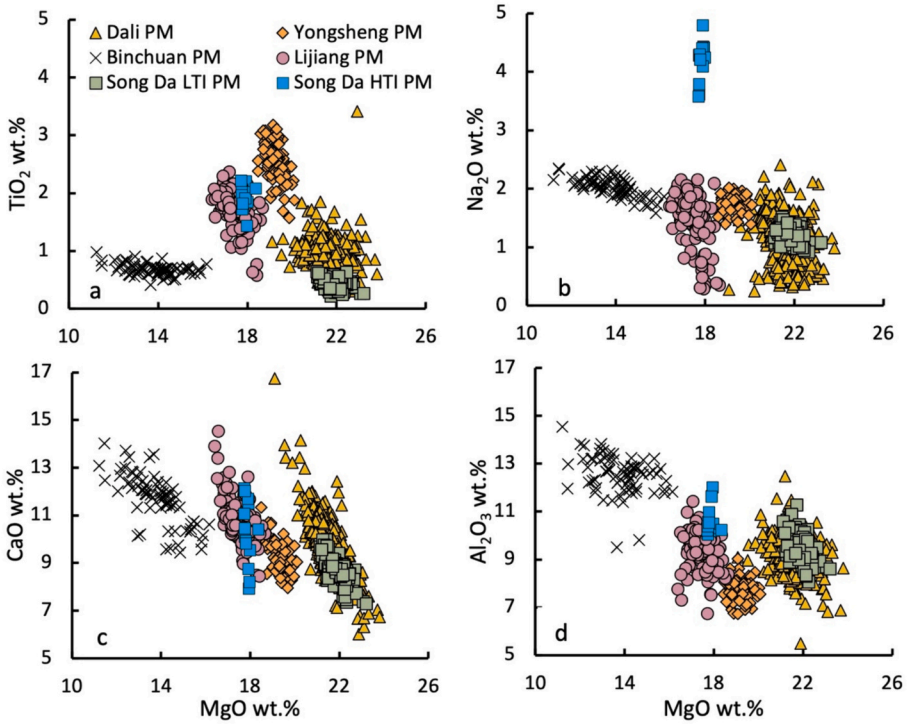

Fig. 8. Estimated parental melt compositions of Emeishan flood basalts from different locations. All data are calculated using Petrolog4 software (https://petrologsoftware.com Danyushevsky and Plechov, 2011) to match equilibrium with the most Fo-rich olivine in each suite. The calculation was done using the model of Ford et al. (1983) except for Song Da low-Ti suite (Song Da LedTi) which was calculated using the model of Danyushevsky (2001) using H_2O contents, and Song Da high-Ti suite (Song Da HTi) using the model of Weaver and Langmuir (1990). Data of Yongsheng and Binchuan melt inclusions are from Kamenetsky et al. (2012). Dali and Lijiang parental melt compositions are from Zhang et al. (2021) and Song Da parental melt composition is from this study.

Sobolev et al., 2016). The second school of thought defended the hypothesis of wet melting of mantle in a subduction zone environment (De Wit and Ashwal, 1997; Grove et al., 1997; Parman et al., 1997, 2003, 2004). The highest temperature recorded for the Song Da low-Ti ultramafic lavas is up to 1450 ± 30 °C (Fig. 9) indicating crystallization within the temperature range of komatiites, significantly higher than the crystallization temperatures of boninites or other subduction-related magmas and magmas not related to mantle plumes (Zhang et al., 2023). The SiO_2 and H_2O contents in the parental melt of the Song Da low-Ti suite are 48–50 wt% and 1 wt%, respectively, which are much lower than typical values for boninites: >52 wt% and > 2 wt% (Sobolev and Danyushevsky, 1994; Dobson et al., 1995; Sobolev and Chaussidon, 1996). Furthermore, $\frac{Cr}{(Cr+Al)}$ values in spinels from the Song Da suite (0.70–0.40) are lower than those of boninites (0.95–0.70) (Sobolev and Danyushevsky, 1994). Finally, Song Da low-Ti lavas completely lack negative Nb anomalies (Fig. 4) characteristic of most supra-subduction zone magmas, including boninites (e.g., Falloon et al., 2008). The above arguments strongly suggest that the low-Ti Song Da lavas were derived from a mantle plume rather than formed in a supra-subduction zone setting.

6.3. The H_2O contents in Song Da ultramafic lavas

Based on the water content of the Song Da low-Ti suite, we identified two different melt inclusions groups, the low-Ti low-H_2O and the low-Ti high-H_2O types. While both types of inclusions are present in each sample, in particular samples one of type dominates (see Fig. 6 caption). This observation could be interpreted as indicating the presence of two different types of magmas; however, two arguments are inconsistent with this explanation: 1) Gavrilenko et al. (2016) showed that the presence of water in the melt decreases the olivine/melt partition coefficient for Ca. Hence, the difference in the water contents in the melts should be reflected in the CaO content of equilibrium olivines. However, as is evident from Fig. 5, there is no difference between the CaO content of the olivines of the high-H_2O and low-H_2O low-Ti suites. 2) The second argument that contradicts the existence of two different types of low-Ti lavas is the Sc/Y ratio of olivine as a proxy of the crystallization temperature (Mallmann and O'Neill, 2013). The presence of water in the melt leads to a decrease in the crystallization temperature for the same forsterite content. But the Sc/Y ratios of host olivines are similar in both low-H_2O and high-H_2O low-Ti melts (Fig. 5). The possible explanation for the origin of the H_2O difference in the low-water group can be the following. During crystallization, the low-H_2O olivine grains may have stayed under a low H_2O pressure (near surface conditions) and high temperature longer than the high- H_2O group, leading to the hydrogen loss from their melt inclusions by diffusion through the host olivine. Such a process is well known and has been reported in several studies (e.g. Sobolev et al., 2019 and references therein).

The reported data suggest that the Song Da low-Ti melts had an elevated H_2O content since the very beginning of their crystallization (Fig. 6): e.g., H_2O of 0.7 wt% is recorded in the melt with MgO of 21.6 wt % included in the most Mg-rich olivine grains with Fo 93.2 (SD22–4-2, Supplementary Table 2). However, the water in Song Da low-Ti ultramafic melt could come from its mantle source or via contamination with hydrated crustal rocks, such as serpentinite, for instance (e.g., Borisova et al., 2020). We think that the second scenario is unlikely because of extremely low contents of elements typical for altered rocks in these melts: average $K_2O = 0.038 \pm 0.004$ (2SE) wt% and average $Cl = 0.003 \pm 0.001$ wt%. This leaves almost no room for detectable contamination with altered crustal rocks. Thus, we conclude that elevated H_2O contents in parental melts of low-Ti ultramafic lavas came from their mantle source, which likely entrained it from the hydrated MTZ passing by in a partially molten state.

The amount of H_2O in the source of low-Ti Song Da melts can be estimated at around 0.17 wt% using 26% degree of melting and 0.64 wt % of H_2O in the primary melt (see section 7.4 below), assuming perfect

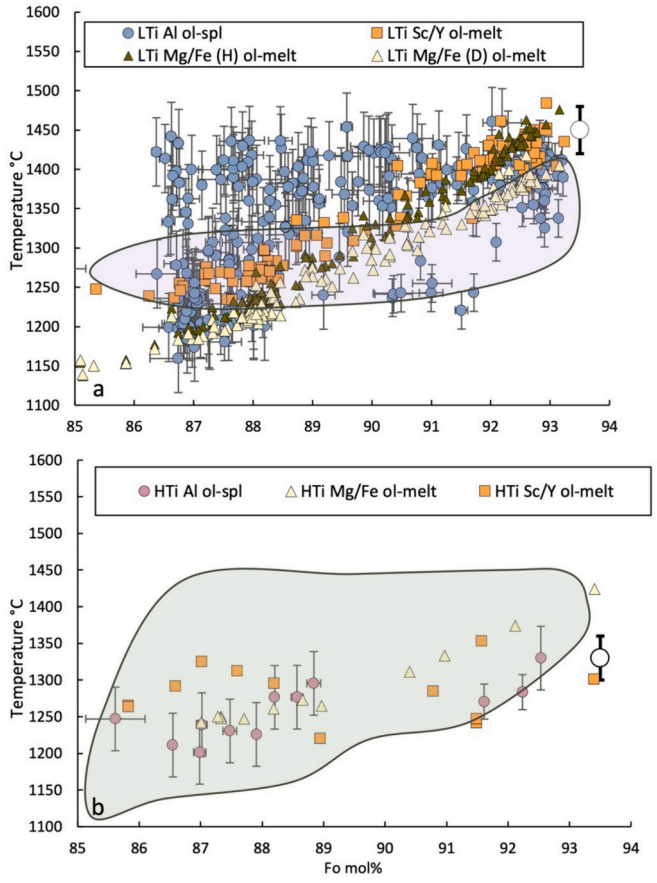

Fig. 9. a) Crystallization temperatures of Song Da low-Ti suite rocks, with the light blue field representing crystallization temperatures of the high-Ti suite. b) Crystallization temperatures of Song Da high-Ti suite rocks, with the light green field representing crystallization temperatures of the low-Ti suite. Crystallization temperature is calculated using three different geothermometers: 1) Al-in-olivine geothermometer (Zhang et al., 2023) represented by circles, 2) Fe—Mg partitioning between olivine and melt inclusions (Ford et al., 1983; Danyushevsky, 2001) represented by yellow triangles, (Herzberg and O'Hara, 2002) represented by dark green triangles, and 3) Sc and Y partitioning between olivine and melt (Mallmann and O'Neill, 2013) represented by squares. All errors are based on 2 standard deviations. LTi = Song Da low-Ti. HTi = Song Da high-Ti. Maximum crystallization temperatures are represented by the large open circles in each diagram. (For interpretation of the references to color in this figure legend, the reader is referred to the web version of this article.)

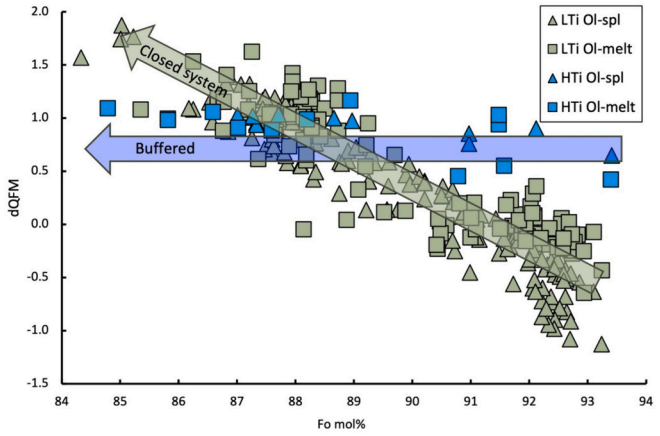

Fig. 10. ΔQFM values representing the oxygen fugacity compared to the quartz–fayalite–magnetite buffer calculated using two different methods: 1) V partitioning between olivine and melt (squares) (Mallmann and O'Neill, 2013). 2) Fe^{2+}/Fe^{3+}(melt) based on olivine and spinel composition (Triangles) (Borisov and Shapkin, 1990). Green symbols represent the low-Ti suite and blue symbols represent the high-Ti suite. LTi = Song Da low-Ti. HTi = Song Da high-Ti. (For interpretation of the references to color in this figure legend, the reader is referred to the web version of this article.)

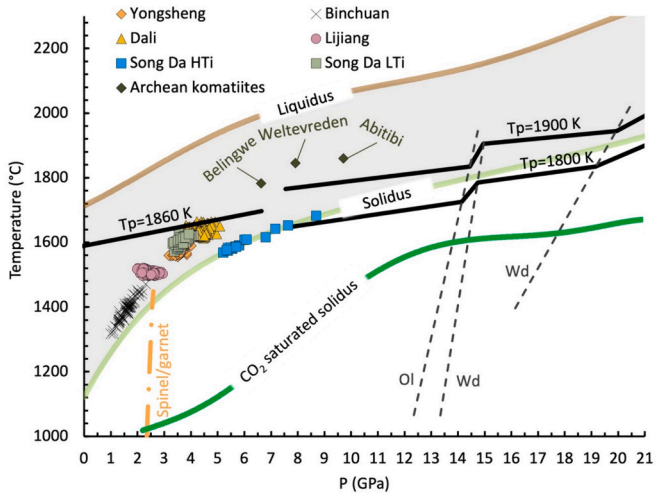

Fig. 11. Melting temperatures and pressures calculated using the model of Lee et al. (2009). Liquidus and solidus curves, phase boundaries in the MTZ, and mantle potential temperature adiabats are from Andrault et al. (2018) except that for Tp = 1860 K, which is based on the extrapolation of Song Da mantle potential temperature. CO_2-saturated solidus (Dasgupta, 2013). Spinel to garnet lherzolite subsolidus transition is from Walter (1998). Song Da LTi = Song Da low-Ti. Song Da HTi = Song Da high-Ti.

incompatibility of H_2O with the restite at 3.7 ± 0.3 GPa (see section 7.4 below). This requires entrainment of around 0.15 wt% of the water from MTZ assuming the initial amount of H_2O in the plume close to 200 ppm. The explanation of the scenario of H_2O entrainment from the MTZ by a partially molten mantle plume is out of the scope of this paper. Here we rely on the hypothesis of Sobolev et al. (2016, 2019), which is based on experimental and natural evidence of a hydrated MTZ and explains well both H_2O excess in extremely hot mantle plumes (e.g., Barberton, Abitibi, Belingwe, Caribbean, and now Emeishan) and the absence of excess H_2O in the magmas from classical Phanerozoic mantle plumes, such as Hawaii or Iceland, which should also pass through the hydrated MTZ. The latter is attributed to their lower temperature, which was not high enough to produce partial melts at the MTZ depths. These plumes thus pass the MTZ in a solid state, which complicates the entrainment of hydrated wadsleyite or melt in the olivine-wadsleyite boundary. Conversely, the melt network in a partially molten plume may facilitate such a process.

The low H_2O contents in melt inclusions of the high-Ti Song Da picrite samples can also be explained by hydrogen loss by volume diffusion or/and by degassing close to Earth's surface.

6.4. *Pressure and potential temperature of mantle sources*

Potential mantle temperatures represent the adiabatic projection of the mantle source temperatures to the surface (McKenzie and Bickle, 1988). They allow to compare different mantle plumes at the same pressure. The water content of the Song Da primary melt is estimated to be up to 1 wt%. The Gorgona and some Archean komatiites show similarly high water contents (Sobolev et al., 2019 and references therein). Assuming that the reconstructed parental melts of the Song Da magmas did not change their composition since equilibration with the mantle source, the temperature, pressure, and potential temperature of the Song Da mantle plume source can be estimated. The model of Lee

et al. (2009) allows to calculate the melting temperature and pressure of these sources based on the composition of the primary melt. We apply this model to our data and published primary melt compositions estimated for other volcanic suites from the Emeishan LIP. However, because of the lack of measured H_2O contents in melt inclusions of other Emeishan lavas, the calculated temperatures and pressures of their primary melts could be overestimated. The results are shown in Fig. 11. The temperature of the mantle source of the Song Da low-Ti suite is around 1610 °C at a pressure of 3.7 ± 0.3 GPa. Together with Dali area melts, the low-Ti Song Da melts show the highest temperatures and degrees of melting for the Emeishan LIP. In contrast, the Song Da high-Ti melts indicate the lowest degrees and highest pressures of melting (at around 1600 °C at 6 ± 2 GPa), though these estimates are less reliable than those for the low-Ti suite because they do not take into account the potentially high CO_2 content of these highly alkaline melts.

Herzberg and Asimow (2015) produced two equations to calculate the potential temperature of a mantle source of a lava. The first equation is based on the crystallization temperature, which in the Song Da case is 1450 ± 30 °C, providing an estimation of the mantle potential temperature for Song Da low-Ti melts at around 1575 °C. The second equation is based on the MgO content of the parental melt that leads to an estimate of 1610 °C for the same suite. The average mantle potential temperature of the Song Da low-Ti suite is thus 1590 °C, falling below the mantle potential temperature estimates of between 1700 and 1850 °C for the Caribbean LIP and Archean komatiites (Sobolev et al., 2016, 2019; Trela et al., 2017; Puchtel et al., 2022). But it is still significantly higher than those of most Phanerozoic mantle plumes (typically lower than 1550 °C, Matthews et al., 2021; Zhang et al., 2023). Also, this temperature is high enough for partial melting of a plume to take place when passing through the MTZ (Andrault et al., 2018), which renders the Song Da low-Ti magmas to be similar to komatiites. It can explain their elevated H_2O contents by its entraining from the hydrated MTZ (Fig. 11). The degree of melting of the mantle source for Song Da low-Ti melts can be estimated by assuming perfect incompatibility of Ti, average Ti of primary melt (2778 ± 78 ppm) and Ti content of the source. For the source composition of the primitive mantle (1086 ppm, Hofmann, 1988), the degree of melting is 39 ± 1%, but for a depleted mantle source (716 ppm, Workman and Hart, 2005), it is 26 ± 1%. Because of the highly radiogenic Nd isotope signature of the Song Da low-Ti lavas (initial ε_{Nd} of up to +8, Hanski et al., 2004), the latter estimate is more realistic. For the Song Da high-Ti suite, the average mantle potential temperature is around 1450 °C, i.e. on the lower end of the range for most Phanerozoic mantle plumes (Matthews et al., 2021; Zhang et al., 2023).

6.5. Origin of the high-Ti picrites

The Emeishan flood basalts are subdivided into three different types: low-Ti, high-Ti, and intermediate-Ti (Kamenetsky et al., 2012). The origin of the high-Ti type has long been under debate. Some authors have proposed that their source is different from that of the low-Ti type (Xiao et al., 2004; Jourdan et al., 2007; Xu et al., 2007). Others argue that the former was derived from the same mantle source, but at a lower degree of melting, at a depth of between 200 and 400 km (Wang et al., 2007; Zhang et al., 2019). Emo and Kamber (2022) suggested that intraplate high-Ti magmas can originate from contamination with material of the lower continental crust. Although the Song Da high-Ti picrite and its olivine-hosted melt inclusions were emplaced on submerged continental crust, continental crust contamination is not compatible with their SiO_2-undersaturation (nepheline present in the groundmass and in norm), enrichment in MgO and high Nb/La and Nb/Th ratios (Fig. 4). We, thus, propose a mantle origin for the Song Da high-Ti picritic melts.

The data obtained in this study indicate that the high-Ti sample is enriched in highly incompatible elements and depleted in heavy REE (Fig. 4), which suggests a lower degree of melting at a high pressure in equilibrium with garnet. The high starting crystallization temperatures (>1300 °C, Fig. 9b) preclude the origin of the high-Ti primary melt within the subcontinental mantle lithosphere. The estimated primary melt composition yields a pressure of 6 ± 2 GPa (around 200 km) and a temperature close to the dry peridotite solidus (Fig. 11). The degree of melting of the mantle source calculated using the Ti content of the Song Da high-Ti primary melt (12,061 ± 1265 ppm) in a similar way done for the low-Ti melts is between 6 and 9%.

This study and the previous works (Anh et al., 2011; Hanski et al., 2004) suggested that the Song Da low-Ti ultramafic lavas represent the most depleted rocks in the LIP with the most forsterite-rich olivines crystallized from high-temperature melts. However, the composition of the mantle source of the high-Ti alkaline melts studied here is not yet constrained. Further investigation of high-Ti samples using melt inclusion and bulk-rock data is required to determine the isotope and trace elements composition of its parental melt.

6.6. Are low-Ti Song Da rocks komatiites?

Viljoen and Viljoen (1969) reported a discovery of highly magnesian volcanic rocks in the Komati River Valley in the Barberton Greenstone Belt, South Africa, and gave them the name “komatiite”. The optimal solution to separate komatiites from the other high-magnesian volcanic rocks was to add the concept of spinifex texture to the definition of komatiites. Brooks and Hart (1974) suggested a new definition that was emphasized by Kerr and Arndt (2001): *“the term komatiite [should] be reserved solely for lavas with characteristic spinifex-textured olivines, or lavas that can be related directly, using field or petrological criteria, to lavas with this texture.”* The apparent reason for such a definition is to distinguish between rocks originated from superheated ultramafic melts from olivine cumulates of basic magmas.

The lack of olivine spinifex texture in the low-Ti Song Da rocks precludes the use of the term komatiites as a nomenclature for these rocks. Also, it should be noted that olivine spinifex textures can also exist in rocks that are chemically far from komatiitic as evidenced by the OIB-like Pechenga ferropicrites or the Boston Creek komatiite (Hanski and Smolkin, 1995; Stone et al., 1995). Nevertheless, based on the data presented earlier, melt inclusion compositions show that the MgO content in the primary melt of the low-Ti Song Da rocks is higher than 18 wt %. In addition, the geothermometry data show that these rocks started to crystallize at temperatures above 1400 °C, which is within the temperature range of komatiite crystallization (Sobolev et al., 2016, 2019; Asafov et al., 2018). Also, low-Ti Song Da lavas are moderately depleted in incompatible elements and are very similar to those of Gorgona komatiites (Fig. 4). Finally, H_2O excess over K_2O in Song Da low-Ti melts is similar to komatiites and differs from other mantle plume-related magmas (Sobolev et al., 2019). Thus, the data presented in this paper show that the Song Da low-Ti lavas share all the features of komatiites except for the olivine spinifex texture. The reason for the absence of such a texture in Song Da low-Ti lavas is relatively low eruption temperature (below 1200 °C, Fig. 9) and thus a low MgO content in the erupted melt (<10 wt%) due to cooling and fractionation of olivine in a plumbing system. With respect to the original definition of komatiites, we can at least suggest that Song Da low-Ti rocks likely originated from a komatiitic melt.

7. Conclusions

1) Detailed study of the mineralogy and geochemistry of bulk-rock samples and olivine-hosted melt and spinel inclusions was performed on ultramafic lavas of the Song Da district, North Vietnam, which represents part of the ca. 260 Ma Emeishan Large Igneous Province. Highly MgO-rich olivine phenocrysts with 93.3–93.4 mol% Fo were found in both low-Ti and high-Ti suites of the Song Da ultramafic lavas.

2) Crystallization conditions of olivine phenocrysts defined by the Al in olivine-spinel, Sc/Y olivine-melt and Fe—Mg olivine-melt geothermometers and by the Fe^{+2}/Fe^{+3} spinel-melt and V olivine-melt oxybarometers are the following. For the Song Da low-Ti rocks, T = 1450–1150 °C and oxygen fugacity evolution in a closed system between ΔQFM -0.5- +1.5; and for the Song Da high-Ti rocks, T = 1320-1200 °C and buffered oxygen fugacity at ΔQFM +0.5–1.0.
3) The MgO content of melt inclusions trapped by 93.3 mol% Fo olivine in Low-Ti lavas between 21 and 23 wt%. The parental melt of these lavas contained around 0.7 wt% H_2O, yielding unusually high H_2O/K_2O ratios of up to 50 times of those in typical mantle sources. The parental melt of high-Ti picrite is undersaturated in silica, enriched in Na (up to 4.8 wt% Na_2O) and contained ca. 17–18 wt% MgO.
4) The primary melts of the Song Da low-Ti suite originated from partial melting of a peridotitic source at around 1610 °C and pressure of 3.7 ± 0.3 GPa. Together with the Dali area melts, the low-Ti Song Da melts are the highest-temperature and degree of melting (>26%) melts for the Emeishan LIP, whereas the Song Da high-Ti melts indicate the lowest degree (<9%) and highest pressure of melting (6.0 ± 2.0 GPa at 1600 °C). The average mantle potential temperature of the Song Da low-Ti suite is ca. 1590 °C, falling below that estimated for the Caribbean LIP and Archean komatiites, but being higher than that for most Phanerozoic mantle plume sources. Also, this temperature is high enough to induce partial melting of a plume when it passed through the MTZ, which makes the Song Da low-Ti magmas similar to komatiites and can explain their elevated H_2O content by entrainment from the hydrated MTZ. For the Song Da high-Ti suite, the average calculated mantle potential temperature is around 1450 °C, which is on the lower end of the range for the majority of Phanerozoic plumes.
5) Many characteristics of low-Ti Song Da suite melts, including their high MgO content (up to 23 wt%), high temperature (up to 1450 °C), elevated H_2O and its excess over K_2O and a depleted nature of the bulk rocks are all consistent with the typical features of komatiitic melts. We, thus, support the conclusion derived from the previous studies that these rocks are related to komatiitic melts of Paleozoic age.

CRediT authorship contribution statement

Charbel Kazzy: Writing – review & editing, Writing – original draft, Visualization, Validation, Formal analysis, Data curation. **Alexander V. Sobolev:** Writing – review & editing, Supervision, Project administration, Funding acquisition, Data curation, Conceptualization. **Valentina G. Batanova:** Writing – review & editing, Validation, Methodology, Formal analysis, Data curation. **Evgeny V. Asafov:** Writing – review & editing, Investigation. **Eero Hanski:** Writing – review & editing, Resources. **Igor S. Puchtel:** Writing – review & editing, Resources. **Andrey E. Izokh:** Resources. **Leonid V. Danyushevsky:** Software, Methodology. **Vũ Hoàng Ly:** Resources. **Can Pham-Ngoc:** Resources. **Tran Tuan Anh:** Resources.

Declaration of competing interest

The authors declare that they have no known competing financial interests or personal relationships that could have appeared to influence the work reported in this paper.

Data availability

All original data presented in supplementary excel file (Appendix A.)

Acknowledgments

This project has received funding from the European Research Council (ERC) under the European Union's Horizon 2020 research and innovation program (grant agreement No 856555). We thank Francis Coeur and Nouméa Boutin-Paradis (GeoThermoChronology Platform, ISTerre) for technical support, N. Arndt for very useful comments on the manuscript, Martine Lanson and Sylvain Campillo for the help in powder preparation, Julien Leger for the assistance on laser ablation ICP-MS and Alexander Chugunov and Alina Koshlyakova for the help on olivine quenching, Maxim Portnyagin for providing glasses for calibration of H_2O by Raman. We thank Dr. Sonja Aulbach for efficient editorial handling and valuable advice and two anonymous reviewers for their feedback and helpful comments on the first version of the manuscript.

Appendix A. Supplementary data

Supplementary data to this article can be found online at https://doi.org/10.1016/j.chemgeo.2024.122219.

References

Ali, J.R., Fitton, J.G., Herzberg, C., 2010. Emeishan large igneous province (SW China) and the mantle-plume up-doming hypothesis. J. Geol. Soc. Lond. 167 (5), 953–959.
Andrault, D., Pesce, G., Manthilake, G., Monteux, J., Bolfan-Casanova, N., Chantel, J., Novella, D., Guignot, N., King, A., Itié, J.-P., 2018. Deep and persistent melt layer in the Archaean mantle. Nat. Geosci. 11 (2), 139–143.
Anh, T.V., Pang, K.-N., Chung, S.-L., Lin, H.-M., Hoa, T.T., Anh, T.T., Yang, H.-J., 2011. The Song Da magmatic suite revisited: A petrologic, geochemical and Sr–Nd isotopic study on picrites, flood basalts and silicic volcanic rocks. J. Asian Earth Sci. 42 (6), 1341–1355. https://doi.org/10.1016/j.jseaes.2011.07.020.
Arndt, N.T., 1977. Ultrabasic magmas and high-degree melting of the mantle. Contrib. Mineral. Petrol. 64 (2), 205–221. https://doi.org/10.1007/BF00371512.
Arndt, N., Brooks, C., 1980. Komatiites. Geology 8 (3), 155–156.
Arndt, N.T., Nisbet, E.G., 1982. What Is a Komatiite? 19—27. Komatiites, George Allen and Unwin, London.
Arndt, N., Ginibre, C., Chauvel, C., Albarede, F., Cheadle, M., Herzberg, C., Jenner, G., Lahaye, Y., 1998. Were komatiites wet? Geology 26 (8), 739–742.
Arndt, N., Lesher, M.C., Barnes, S.J., 2008. Komatiite. Cambridge university press.
Asafov, E.V., Sobolev, A.V., Gurenko, A.A., Arndt, N.T., Batanova, V.G., Portnyagin, M.V., Garbe-Schönberg, D., Krasheninnikov, S.P., 2018. Belingwe komatiites (2.7 Ga) originate from a plume with moderate water content, as inferred from inclusions in olivine. Chem. Geol. 478, 39–59.
Asafov, E.V., Sobolev, A.V., Batanova, V.G., Portnyagin, M.V., 2020. Chlorine in the Earth's Mantle as an Indicator of the Global Recycling of Oceanic Crust. Russ. Geol. Geophys. 61 (9), 937–950.
Balykin, P.A., Petrova, T.E., 2000. Petrological types and genesis of komatiite-basalt, picrite-basalt, and picrite-dolerite complexes. Geol. Geofiz. 41 (8), 1098–1111.
Balykin, P.A., Polyakov, G.V., Petrova, T.E., Hoang Huu Thanh, T.T.H., Ngo Thi Phuong, T.Q.H., 1996. Petrology and evolution of the formation of Permian-Triassic mafic-ultramafic associations in North Vietnam. J. Geol. Ser. B 7, 59–64.
Balykin, P.A., Polyakov, G.V., Izokh, A.E., Hoa, T.T., Phuong, N.T., Hung, T.Q., Petrova, T.E., 2010. Geochemistry and petrogenesis of Permian ultramafic-mafic complexes of the Jinping–Song Da rift (southeastern Asia). Russ. Geol. Geophys. 51 (6), 611–624.
Batanova, V.G., Belousov, I.A., Savelieva, G.N., Sobolev, A.V., 2011. Consequences of channelized and diffuse melt transport in supra-subduction zone mantle: evidence from the Voykar Ophiolite (Polar Urals). J. Petrol. 52 (12), 2483–2521.
Batanova, V.G., Sobolev, A.V., Kuzmin, D.V., 2015. Trace element analysis of olivine: High precision analytical method for JEOL JXA-8230 electron probe microanalyser. Chem. Geol. 419, 149–157. https://doi.org/10.1016/j.chemgeo.2015.10.042.
Batanova, V.G., Sobolev, A.V., Magnin, V., 2018. Trace element analysis by EPMA in geosciences: Detection limit, precision and accuracy. IOP Conf. Ser. 304, 012001 https://doi.org/10.1088/1757-899X/304/1/012001.
Batanova, V.G., Thompson, J.M., Danyushevsky, L.V., Portnyagin, M.V., Garbe-Schönberg, D., Hauri, E., Kimura, J.-I., Chang, Q., Senda, R., Goemann, K., Chauvel, C., Campillo, S., Ionov, D.A., Sobolev, A.V., 2019. New olivine reference material for in situ microanalysis. Geostand. Geoanal. Res. 43 (3), 453–473. https://doi.org/10.1111/ggr.12266.
Borisov, A.A., Shapkin, A.I., 1990. A new empirical equation rating Fe3+/Fe2+ in magmas to their composition, oxygen fugacity, and temperature. Geochem. Int. 27 (1), 111–116.
Borisova, A.Y., Zagrtdenov, N.R., Toplis, M.J., Ceuleneer, G., Safonov, O.G., Pokrovski, G.S., Jochum, K.P., Stoll, B., Weis, U., Shcheka, S., 2020. Hydrated peridotite–basaltic melt interaction Part II: Fast assimilation of serpentinized mantle by basaltic magma. Front. Earth Sci. 8, 84.
Brooks, C., Hart, S.R., 1974. On the significance of komatiite. Geology 2 (2), 107–110.
Campbell, I.H., Griffiths, R.W., 1992. The changing nature of mantle hotspots through time: implications for the chemical evolution of the mantle. J. Geol. 100 (5), 497–523. https://doi.org/10.1086/629605.
Campbell, I.H., Griffiths, R.W., Hill, R.I., 1989. Melting in an Archaean mantle plume: Heads it's basalts, tails it's komatiites. Nature 339 (6227), 697–699.
Chung, S.-L., Lee, T.-Y., Lo, C.-H., Wang, P.-L., Chen, C.-Y., Yem, N.T., Hoa, T.T., Genyao, W., 1997. Intraplate extension prior to continental extrusion along the Ailao Shan-Red River shear zone. Geology 25 (4), 311–314.

Chung, S.-L., Jahn, B.-M., Genyao, W., Lo, C.-H., Bolin, C., 1998. The Emeishan flood basalt in SW China: A mantle plume initiation model and its connection with continental breakup and mass extinction at the Permian-Triassic boundary. In: Mantle Dynamics and Plate Interactions in East Asia, 27, pp. 47–58.
Danyushevsky, L.V., 2001. The effect of small amounts of H2O on crystallisation of mid-ocean ridge and backarc basin magmas. J. Volcanol. Geotherm. Res. 110 (3–4), 265–280.
Danyushevsky, L.V., Plechov, P., 2011. Petrolog3: Integrated software for modeling crystallization processes. Geochem. Geophys. Geosyst. 12 (7).
Danyushevsky, L.V., Della-Pasqua, F.N., Sokolov, S., 2000. Re-equilibration of melt inclusions trapped by magnesian olivine phenocrysts from subduction-related magmas: Petrological implications. Contrib. Mineral. Petrol. 138 (1), 68–83.
Danyushevsky, L.V., McNeill, A.W., Sobolev, A.V., 2002. Experimental and petrological studies of melt inclusions in phenocrysts from mantle-derived magmas: an overview of techniques, advantages and complications. Chem. Geol. 183 (1–4), 5–24.
Dasgupta, R., 2013. Ingassing, storage, and outgassing of terrestrial carbon through geologic time. Rev. Mineral. Geochem. 75 (1), 183–229.
De Wit, M.J., Ashwal, L.D., 1997. Greenstone Belts. Clarendon Press. https://books.google.fr/books?id=IcMSAQAAIAAJ.
Dixon, J.E., Bindeman, I.N., Kingsley, R.H., Simons, K.K., Le Roux, P.J., Hajewski, T.R., Swart, P., Langmuir, C.H., Ryan, J.G., Walowski, K.J., Wada, I., Wallace, P.J., 2017. Light stable isotopic compositions of enriched mantle sources: resolving the dehydration paradox. Geochem. Geophys. Geosyst. 18 (11), 3801–3839. https://doi.org/10.1002/2016GC006743.
Dobson, P.F., Skogby, H., Rossman, G.R., 1995. Water in boninite glass and coexisting orthopyroxene: Concentration and partitioning. Contrib. Mineral. Petrol. 118 (4), 414–419.
Echeverria, L.M., 1980. Tertiary or Mesozoic komatiites from Gorgona Island, Colombia: field relations and geochemistry. Contrib. Mineral. Petrol. 73 (3), 253–266.
Emo, R.B., Kamber, B.S., 2022. Linking granulites, intraplate magmatism, and bi-mineralic eclogites with a thermodynamic-petrological model of melt-solid interaction at the base of anorogenic lower continental crust. Earth Planet. Sci. Lett. 594, 117742.
Falloon, T.J., Danyushevsky, L.V., Crawford, A.J., Meffre, S., Woodhead, J.D., Bloomer, S.H., 2008. Boninites and adakites from the northern termination of the Tonga Trench: implications for adakite petrogenesis. J. Petrol. 49 (4), 697–715.
Faure, F., Arndt, N., Libourel, G., 2006. Formation of spinifex texture in komatiites: an experimental study. J. Petrol. 47 (8), 1591–1610.
Ford, C.E., Russell, D.G., Groven, J.A., Fisk, M.R., 1983. Distribution coefficients of Mg2+, Fe2+, Ca2+ and Mn2+ between olivine and melt. J. Petrol. 24, 256–265.
Gavrilenko, M., Herzberg, C., Vidito, C., Carr, M.J., Tenner, T., Ozerov, A., 2016. A calcium-in-olivine geohygrometer and its application to subduction zone magmatism. J. Petrol. 57 (9), 1811–1832.
Grove, T.L., De Wit, M.J., Dann, J.C., 1997. Komatiites from the komati type section, Barberton, South Africa. Oxf. Monogr. Geol. Geophys. 35 (1), 438–456.
Gurenko, A.A., Kamenetsky, V.S., Kerr, A.C., 2016. Oxygen isotopes and volatile contents of the Gorgona komatiites, Colombia: A confirmation of the deep mantle origin of H2O. Earth Planet. Sci. Lett. 454, 154–165.
Hanski, E.J., Smolkin, V.F., 1995. Iron- and LREE-enriched mantle source for early Proterozoic intraplate magmatism as exemplified by the Pechenga ferropicrites, Kola Peninsula, Russia. Lithos 34 (1), 107–125. https://doi.org/10.1016/0024-4937(95)90015-2.
Hanski, E., Walker, R.J., Huhma, H., Polyakov, G.V., Balykin, P.A., Hoa, T.T., Phuong, N.T., 2004. Origin of the Permian-Triassic komatiites, northwestern Vietnam. Contrib. Mineral. Petrol. 147 (4), 453–469.
Hanski, E., Kamenetsky, V.S., Luo, Z.-Y., Xu, Y.-G., Kuzmin, D.V., 2010. Primitive magmas in the Emeishan large igneous province, southwestern China and northern Vietnam. Lithos 119 (1–2), 75–90.
Hauri, E., 2002. SIMS analysis of volatiles in silicate glasses, 2: Isotopes and abundances in Hawaiian melt inclusions. Chem. Geol. 183 (1–4), 115–141.
Herzberg, C., 1992. Depth and degree of melting of komatiites. J. Geophys. Res. Solid Earth 97 (B4), 4521–4540. https://doi.org/10.1029/91JB03066.
Herzberg, C., 1995. Generation of plume magmas through time: an experimental perspective. Chem. Geol. 126 (1), 1–16.
Herzberg, C., Asimow, P.D., 2015. PRIMELT 3 MEGA. XLSM software for primary magma calculation: Peridotite primary magma MgO contents from the liquidus to the solidus. Geochem. Geophys. Geosyst. 16 (2), 563–578.
Herzberg, C., O'Hara, M.J., 2002. Plume-associated ultramafic magmas of Phanerozoic age. J. Petrol. 43 (10), 1857–1883.
Herzberg, C., Condie, K., Korenaga, J., 2010. Thermal history of the Earth and its petrological expression. Earth Planet. Sci. Lett. 292 (1–2), 79–88.
Hofmann, A.W., 1988. Chemical differentiation of the Earth: the relationship between mantle, continental crust, and oceanic crust. Earth Planet. Sci. Lett. 90 (3), 297–314.
Izokh, A.E., Polyakov, G.V., Hoa, T.T., Balykin, P.A., Phuong, N.T., 2005. Permian-Triassic ultramafic-mafic magmatism of northern Vietnam and southern China as expression of plume magmatism. Russ. Geol. Geophys. 46 (9), 922–932.
Jourdan, F., Bertrand, H., Schärer, U., Blichert-Toft, J., Féraud, G., Kampunzu, A.B., 2007. Major and trace element and Sr, Nd, Hf, and Pb isotope compositions of the Karoo large igneous province, Botswana–Zimbabwe: Lithosphere vs mantle plume contribution. J. Petrol. 48 (6), 1043–1077.
Kamenetsky, V.S., Gurenko, A.A., Kerr, A.C., 2010. Composition and temperature of komatiite melts from Gorgona Island, Colombia, constrained from olivine-hosted melt inclusions. Geology 38 (11), 1003–1006.
Kamenetsky, V.S., Chung, S.-L., Kamenetsky, M.B., Kuzmin, D.V., 2012. Picrites from the Emeishan large Igneous Province, SW China: A compositional continuum in primitive magmas and their respective mantle sources. J. Petrol. 53 (10), 2095–2113.
Kerr, A.C., Arndt, N.T., 2001. A note on the IUGS reclassification of the high-Mg and picritic volcanic rocks. J. Petrol. 42 (11), 2169–2171.
Koshlyakova, A.N., Sobolev, A.V., Krasheninnikov, S.P., Batanova, V.G., Borisov, A.A., 2022. Ni partitioning between olivine and highly alkaline melts: an experimental study. Chem. Geol. 587, 120615.
Labrosse, S., 2002. Hotspots, mantle plumes and core heat loss. Earth Planet. Sci. Lett. 199 (1–2), 147–156.
Lan, C.-Y., Chung, S.-L., Jiun-San Shen, J., Lo, C.-H., Wang, P.-L., Hoa, T.T., Thanh, H.H., Mertzman, S.A., 2000. Geochemical and Sr–Nd isotopic characteristics of granitic rocks from northern Vietnam. J. Asian Earth Sci. 18 (3), 267–280.
Lan, C.-Y., Chung, S.-L., Lo, C.-H., Lee, T.-Y., Wang, P.-L., Li, H., Van Toan, D., 2001. First evidence for Archean continental crust in northern Vietnam and its implications for crustal and tectonic evolution in Southeast Asia. Geology 29 (3), 219–222.
Lee, C.-T.A., Luffi, P., Plank, T., Dalton, H., Leeman, W.P., 2009. Constraints on the depths and temperatures of basaltic magma generation on Earth and other terrestrial planets using new thermobarometers for mafic magmas. Earth Planet. Sci. Lett. 279 (1–2), 20–33.
Liu, Y., Hu, Z., Gao, S., Günther, D., Xu, J., Gao, C., Chen, H., 2008. In situ analysis of major and trace elements of anhydrous minerals by LA-ICP-MS without applying an internal standard. Chem. Geol. 257 (1–2), 34–43.
Longerich, H.P., Jackson, S.E., Gunther, D., 1996. Laser ablation inductively coupled plasma mass spectrometric transient signal data acquisition and analyte concentration calculation. J. Anal. At. Spectrom. 11, 899-904..
Loper, D.E., Lay, T., 1995. The core-mantle boundary region. J. Geophys. Res. Solid Earth 100 (B4), 6397–6420. https://doi.org/10.1029/94JB02048.
Mallmann, G., O'Neill, H.S.C., 2013. Calibration of an empirical thermometer and oxybarometer based on the partitioning of Sc, Y and V between olivine and silicate melt. J. Petrol. 54 (5), 933–949.
Matthews, S., Wong, K., Shorttle, O., Edmonds, M., Maclennan, J., 2021. Do olivine crystallization temperatures faithfully record mantle temperature variability? Geochem. Geophys. Geosyst. 22 (4), e2020GC009157 https://doi.org/10.1029/2020GC009157.
Maurel, C., Maurel, P., 1984. Etude expérimentale de la distribution du fer ferrique entre spinelle chromifère et bain silicaté basique. Bull. Mineral. 107 (1), 25–33.
McDonough, W.F., Ireland, T.R., 1993. Intraplate origin of komatiites inferred from trace elements in glass inclusions. Nature 365 (6445), 432–434.
McKenzie, D.A.N., Bickle, M.J., 1988. The volume and composition of melt generated by extension of the lithosphere. J. Petrol. 29 (3), 625–679.
Metcalfe, I., 2002. Permian tectonic framework and palaeogeography of SE Asia. J. Asian Earth Sci. 20 (6), 551–566.
Nam, T.N., Toriumi, M., Sano, Y., Terada, K., Thang, T.T., 2003. 2.9, 2.36, and 1.96 Ga zircons in orthogneiss south of the Red River shear zone in Viet Nam: evidence from SHRIMP U–Pb dating and tectonothermal implications. J. Asian Earth Sci. 21 (7), 743–753.
Nicklas, R.W., Puchtel, I.S., Ash, R.D., Piccoli, P.M., Hanski, E., Nisbet, E.G., Waterton, P., Pearson, D.G., Anbar, A.D., 2019. Secular mantle oxidation across the Archean-Proterozoic boundary: evidence from V partitioning in komatiites and picrites. Geochim. Cosmochim. Acta 250, 49–75.
Nisbet, E.G., Cheadle, M.J., Arndt, N.T., Bickle, M.J., 1993. Constraining the potential temperature of the Archaean mantle: A review of the evidence from komatiites. Lithos 30 (3–4), 291–307.
Norris, A., Danyushevsky, L., 2018. Towards Estimating the Complete Uncertainty Budget of Quantified Results Measured by LA-ICP-MS. Goldschmidt, Boston, MA, USA.
Parman, S.W., Dann, J.C., Grove, T.L., De Wit, M.J., 1997. Emplacement conditions of komatiite magmas from the 3.49 Ga Komati Formation, Barberton greenstone belt, South Africa. Earth Planet. Sci. Lett. 150 (3–4), 303–323.
Parman, S.W., Shimizu, N., Grove, T.L., Dann, J.C., 2003. Constraints on the pre-metamorphic trace element composition of Barberton komatiites from ion probe analyses of preserved clinopyroxene. Contrib. Mineral. Petrol. 144, 383–396.
Parman, S.W., Grove, T.L., Dann, J.C., de Wit, M.J., 2004. A subduction origin for komatiites and cratonic lithospheric mantle. S. Afr. J. Geol. 107 (1–2), 107–118. https://doi.org/10.2113/107.1-2.107.
Polyakov, G.V., Balykin, P.A., Glotov, A.I., Hung, T.Q., Phuong, N.T., Thanh, H.H., Nien, B.A., 1991. Permian–Triassic association of high-magnesian volcanic rocks of the Song Da zone (north-western Vietnam). Sov. Geol. Geophys. 32 (1), e11.
Polyakov, G.V., Balykin, P.A., Tran Trong Hoa, H.H.T., Tran Quoc Hung, N.T.P., Petrova, T.E., Vu Van Van, B.A.N., Tran Tuan Anh, H.V.H., 1996. Permian-Triassic Mafic-Ultramafic Associations of Northern Vietnam. Science and Technics Publishing House, Hanoi, p. 172.
Polyakov, G.V., Balykin, P.A., Hoa, T.T., Phuong, N.T., Thanh, H.H., Hung, C.Q., Ponomarchuk, V.A., Lebedev, Y.N., Kireev, A.D., 1998. Evolution of the Mesozoic-Cenozoic magmatism of the Song Da rift and its contouring structures. Geol. Geofiz. 39 (6), 695–706.
Puchtel, I., Arndt, N., 2024. Archean to recent komatiites and basalts. https://doi.org/10.1016/B978-0-323-99762-1.00065-6.
Puchtel, I.S., Blichert-Toft, J., Horan, M.F., Touboul, M., Walker, R.J., 2022. The komatiite testimony to ancient mantle heterogeneity. Chem. Geol. 594, 120776.
Ren, Z.-Y., Wu, Y.-D., Zhang, L., Nichols, A.R., Hong, L.-B., Zhang, Y.-H., Zhang, Y., Liu, J.-Q., Xu, Y.-G., 2017. Primary magmas and mantle sources of Emeishan basalts constrained from major element, trace element and Pb isotope compositions of olivine-hosted melt inclusions. Geochim. Cosmochim. Acta 208, 63–85.
Rost, S., Garnero, E.J., Williams, Q., Manga, M., 2005. Seismological constraints on a possible plume root at the core–mantle boundary. Nature 435 (7042), 666–669.

Ryabov, V.V., Konenko, V.F., Khmelnikova, O.S., 1985. Rock-forming minerals of picritic basalts of the Noril'sk region. Sov. Geol. Geophys. 26 (4), 77–84.
Shellnutt, J.G., 2014. The Emeishan large igneous province: A synthesis. Geosci. Front. 5 (3), 369–394.
Shimizu, K., Komiya, T., Hirose, K., Shimizu, N., Maruyama, S., 2001. Cr-spinel, an excellent micro-container for retaining primitive melts–implications for a hydrous plume origin for komatiites. Earth Planet. Sci. Lett. 189 (3–4), 177–188.
Sobolev, A.V., 1996. Melt inclusions in minerals as a source of principle petrological information. Petrology 4 (3), 209–220.
Sobolev, A.V., Chaussidon, M., 1996. H2O concentrations in primary melts from supra-subduction zones and mid-ocean ridges: Implications for H2O storage and recycling in the mantle. Earth Planet. Sci. Lett. 137 (1), 45–55. https://doi.org/10.1016/0012-821X(95)00203-O.
Sobolev, A.V., Danyushevsky, L.V., 1994. Petrology and geochemistry of boninites from the north termination of the Tonga Trench: Constraints on the generation conditions of primary high-ca boninite magmas. J. Petrol. 35 (5), 1183–1211.
Sobolev, A.V., Hofmann, A.W., Kuzmin, D.V., Yaxley, G.M., Arndt, N.T., Chung, S.-L., Danyushevsky, L.V., Elliott, T., Frey, F.A., Garcia, M.O., 2007. The amount of recycled crust in sources of mantle-derived melts. Science 316 (5823), 412–417.
Sobolev, A.V., Asafov, E.V., Gurenko, A.A., Arndt, N.T., Batanova, V.G., Portnyagin, M. V., Garbe-Schönberg, D., Krasheninnikov, S.P., 2016. Komatiites reveal a hydrous Archaean deep-mantle reservoir. Nature 531 (7596), 628–632.
Sobolev, A.V., Asafov, E.V., Gurenko, A.A., Arndt, N.T., Batanova, V.G., Portnyagin, M. V., Garbe-Schönberg, D., Wilson, A.H., Byerly, G.R., 2019. Deep hydrous mantle reservoir provides evidence for crustal recycling before 3.3 billion years ago. Nature 571 (7766), 555–559.
Sossi, P.A., Eggins, S.M., Nesbitt, R.W., Nebel, O., Hergt, J.M., Campbell, I.H., O'Neill, H. S.C., Van Kranendonk, M., Davies, D.R., 2016. Petrogenesis and geochemistry of Archean komatiites. J. Petrol. 57 (1), 147–184.
Spandler, C., O'Neill, H.S.C., 2010. Diffusion and partition coefficients of minor and trace elements in San Carlos olivine at 1,300 C with some geochemical implications. Contrib. Mineral. Petrol. 159, 791–818.
Stone, W.E., Crocket, J.H., Dickin, A.P., Fleet, M.E., 1995. Origin of Archean ferropicrites: Geochemical constraints from the Boston Creek Flow, Abitibi greenstone belt, Ontario, Canada. Chem. Geol. 121 (1–4), 51–71.
Sweeney, R.J., Falloon, T.J., Green, D.H., Tatsumi, Y., 1991. The mantle origins of Karoo picrites. Earth Planet. Sci. Lett. 107 (2), 256–271. https://doi.org/10.1016/0012-821X(91)90075-S.
Tang, Q., Li, C., Zhang, M., Lin, Y., 2015. U–Pb age and Hf isotopes of zircon from basaltic andesite and geochemical fingerprinting of the associated picrites in the Emeishan large igneous province, SW China. Mineral. Petrol. 109 (1), 103–114. https://doi.org/10.1007/s00710-014-0349-z.
Tran, T.H., Izokh, A.E., Polyakov, G.V., Borisenko, A.S., Anh, T.T., Balykin, P.A., Phuong, N.T., Rudnev, S.N., Van, V.V., Nien, B.A., 2008. Permo-Triassic magmatism and metallogeny of Northern Vietnam in relation to the Emeishan plume. Russ. Geol. Geophys. 49 (7), 480–491.
Tran, T.H., Lan, C.-Y., Usuki, T., Shellnutt, J.G., Pham, T.D., Tran, T.A., Pham, N.C., Ngo, T.P., Izokh, A.E., Borisenko, A.S., 2015. Petrogenesis of late Permian silicic rocks of Tu Le basin and Phan Si Pan uplift (NW Vietnam) and their association with the Emeishan large igneous province. J. Asian Earth Sci. 109, 1–19.
Trela, J., Gazel, E., Sobolev, A.V., Moore, L., Bizimis, M., Jicha, B., Batanova, V.G., 2017. The hottest lavas of the Phanerozoic and the survival of deep Archaean reservoirs. Nat. Geosci. 10 (6), 451–456.
Usuki, T., Lan, C.-Y., Tran, T.H., Pham, T.D., Wang, K.-L., Shellnutt, G.J., Chung, S.-L., 2015. Zircon U–Pb ages and Hf isotopic compositions of alkaline silicic magmatic rocks in the Phan Si Pan-Tu Le region, northern Vietnam: Identification of a displaced western extension of the Emeishan Large Igneous Province. J. Asian Earth Sci. 97, 102–124.
Viljoen, M.J., Viljoen, R., 1969. The geology and geochemistry of the lower ultramafic unit of the Onverwacht Group and a proposed new class of igneous rocks. Geol. Soc. S. Afr. Spec. Publ. 2, 55–86.
Walter, M.J., 1998. Melting of garnet peridotite and the origin of komatiite and depleted lithosphere. J. Petrol. 39 (1), 29–60.
Wang, C.Y., Zhou, M.-F., Qi, L., 2007. Permian flood basalts and mafic intrusions in the Jinping (SW China)–Song Da (northern Vietnam) district: Mantle sources, crustal contamination and sulfide segregation. Chem. Geol. 3 (243), 317–343.
Waterton, P., Arndt, N., 2023. Komatiites: Their geochemistry and origins. https://earth arxiv.org/repository/view/5969/.
Weaver, J.S., Langmuir, C.H., 1990. Calculation of phase equilibrium in mineral-melt systems. Comput. Geosci. 16 (1), 1–19.
Workman, R.K., Hart, S.R., 2005. Major and trace element composition of the depleted MORB mantle (DMM). Earth Planet. Sci. Lett. 231 (1–2), 53–72.
Xiao, L., Xu, Y.G., Mei, H.J., Zheng, Y.F., He, B., Pirajno, F., 2004. Distinct mantle sources of low-Ti and high-Ti basalts from the western Emeishan large igneous province, SW China: Implications for plume–lithosphere interaction. Earth Planet. Sci. Lett. 228 (3–4), 525–546.
Xu, Y., Chung, S.-L., Jahn, B., Wu, G., 2001. Petrologic and geochemical constraints on the petrogenesis of Permian–Triassic Emeishan flood basalts in southwestern China. Lithos 58 (3), 145–168. https://doi.org/10.1016/S0024-4937(01)00055-X.
Xu, J.-F., Suzuki, K., Xu, Y.-G., Mei, H.-J., Li, J., 2007. Os, Pb, and Nd isotope geochemistry of the Permian Emeishan continental flood basalts: Insights into the source of a large igneous province. Geochim. Cosmochim. Acta 71 (8), 2104–2119.
Zhang, L., Ren, Z.-Y., Handler, M.R., Wu, Y.-D., Zhang, L., Qian, S.-P., Xia, X.-P., Yang, Q., Xu, Y.-G., 2019. The origins of high-Ti and low-Ti magmas in large igneous provinces, insights from melt inclusion trace elements and Sr-Pb isotopes in the Emeishan large igneous province. Lithos 344, 122–133.
Zhang, L., Ren, Z.-Y., Zhang, L., Wu, Y.-D., Qian, S.-P., Xia, X.-P., Xu, Y.-G., 2021. Nature of the mantle plume under the Emeishan large igneous province: Constraints from olivine-hosted melt inclusions of the Lijiang picrites. J. Geophys. Res. Solid Earth 126 (5), e2020JB021022.
Zhang, Y., Namur, O., Li, W., Shorttle, O., Gazel, E., Jennings, E., Thy, P., Grove, T.L., Charlier, B., 2023. An extended calibration of the olivine–spinel aluminum exchange thermometer: Application to the melting conditions and mantle lithologies of large igneous provinces. J. Petrol. 64 (11) egad077.